

Distribution and fluxes of marine particles in the South China Sea continental slope: implications for carbon export

Shujin Guo^{1,2†}, Mingliang Zhu^{1,2†}, Wenlong Xu³, Shan Zheng^{1,2}, Sumei Liu⁴, Ying Wu⁵, Juan Du^{1,2}, Chenhao Zhao¹, Xiaoxia Sun^{1,2,6}

5 ¹Jiaozhou Bay National Marine Ecosystem Research Station, Institute of Oceanology, Chinese Academy of Sciences, Qingdao 266071, China

²Laboratory for Marine Ecology and Environmental Science, Qingdao Marine Science and Technology Center, Qingdao 266237, China

³Ocean College, Jiangsu University of Science and Technology, Zhenjiang 212100, China

10 ⁴Frontiers Science Center for Deep Ocean Multispheres and Earth System, and Key Laboratory of Marine Chemistry Theory and Technology, Ministry of Education, Ocean University of China, Qingdao 266100, China

⁵State Key Laboratory of Estuarine and Coastal Research, Faculty of Earth Sciences, East China Normal University, Shanghai 201100, China

⁶University of Chinese Academy of Sciences, Beijing 100049, China

15 *Correspondence to:* Xiaoxia Sun (xsun@qdio.ac.cn)

Abstract. Marine particles are key vectors in the ocean's biological carbon pump, yet their distribution, size structure, contributions to particulate organic carbon (POC) flux, and the mechanisms controlling these processes remain poorly understood in marginal seas. In this study, we investigated the spatial distribution and carbon flux of marine particles along the continental slope of the South China Sea (SCS), using *in situ* imaging data collected by an Underwater Vision Profiler (UVP-5-HD) during a June 2015 cruise. We also examined how these particle-related processes respond to mesoscale eddy activity. Particle abundance and volume concentration (PVC) ranged from 0 to 783 particles L⁻¹ (mean ± SD: 68 ± 69 particles L⁻¹) and from 0 to 6.7 mm³ L⁻¹ (mean ± SD: 0.3 ± 0.4 mm³ L⁻¹), respectively. Small particles—defined as those with an equivalent spherical diameter (ESD) less than 500 μm—overwhelmingly dominated in terms of abundance, accounting for more than 97% of total counts. However, in terms of PVC, large particles contributed a greater share, averaging 61% ± 12%. PVC was significantly higher in the epipelagic layer (mean ± SD: 0.4 ± 0.7 mm³ L⁻¹) than in the mesopelagic layer (mean ± SD: 0.2 ± 0.1 mm³ L⁻¹, *p* < 0.01), indicating enhanced particle production in surface waters. Under the influence of mesoscale eddies, distinct differences in particle characteristics and carbon export were observed. Cyclonic eddies enhanced particle concentrations and favored the formation of large particles, while anticyclonic eddies were associated with a higher proportion of small particles. These patterns were linked to eddy-induced changes in nutrient availability and phytoplankton production. Consequently, POC fluxes in cyclonic eddy-influenced regions were consistently higher than those in anticyclonic regions throughout the water column, with POC fluxes reaching over twice the magnitude observed in anticyclonic eddy regions. This suggests that mesoscale eddies can influence carbon export by altering both the concentration and size composition of marine particles. Our study clarifies the distribution and size structure of marine particles along the SCS slope and highlights the importance of mesoscale physical processes in regulating particle-mediated carbon export, [thereby enhancing our understanding of carbon cycling processes in dynamic marginal seas, offering useful references for improving carbon export parameterizations in biogeochemical models.](#)

† These authors contributed equally to this work.

Key words: marine particles, Underwater Vision Profiler, particle distribution, size structure, mesoscale eddies, carbon export, South China Sea, continental slope

1 Introduction

Marine particles are critical components of the oceanic carbon cycle, serving as vehicles for transporting organic carbon from the surface ocean to the deep sea via the biological pump (Boyd et al., 2019; Siegel et al., 2022). These particles, which include a diverse array of forms such as micron-scale phytoplankton cells, submillimeter detrital fragments, millimeter-scale aggregates, and zooplankton fecal pellet, play an essential role in global carbon dynamics (Turner, 2015). The abundance and distribution of marine particles are regulated by a combination of abiotic and biotic factors, such as primary productivity, particle aggregation and fragmentation, as well as hydrodynamic conditions all interact to shape particle fields in the ocean (Forest et al., 2012; Kiko et al., 2022). Due to the widespread vertical settling behavior of particles in the ocean, their abundance and size not only influence the efficiency of the carbon export but also govern the biogeochemical pathways through which carbon is transformed, remineralized, or permanently stored in the ocean's interior (Kiko et al., 2022). Therefore, understanding the distribution, size structure, and associated carbon export of marine particles is critical for assessing the efficiency of the biological carbon pump.

Although marine particles play a crucial role in ocean biogeochemical cycles, their fragile nature poses significant challenges for collection and analysis. Sediment traps have been widely employed to capture settling particles and quantify vertical fluxes (Honjo et al., 2008; Harms et al., 2021). While this method provides valuable insights, it lacks the spatial coverage and detailed particle size distribution data necessary for a mechanistic understanding of particle dynamics (Wang et al., 2024a). In recent years, advancements in *in situ* optical and imaging technologies have introduced an alternative approach for assessing particle distribution and estimating fluxes (Picheral et al., 2010; Boss et al., 2015). The Underwater Vision Profiler (UVP) has emerged as a powerful tool, enabling high-resolution, *in situ* measurements of particle abundance and size distribution across a broad depth range (Picheral et al., 2010). ~~The compact design of the UVP allows for integration with conductivity, temperature, and depth (CTD) rosette samplers as well as deployment on small autonomous platforms such as underwater gliders (Picheral et al., 2022).~~ When combined with image processing techniques for particle identification, the UVP facilitates comprehensive characterization of particle abundance, size, composition, and potential sources (Trudnowska et al., 2021, 2023), thereby enhancing our understanding of particle formation and transformation processes. Beyond particle characterization, the UVP has been instrumental in estimating particle fluxes by leveraging empirical relationships between particle size and sinking flux (Guidi et al., 2008a; Iversen et al., 2010; Ramondenc et al., 2016). The high vertical resolution of UVP observations in marine particles, coupled with established size-dependent relationships for carbon content and sinking velocity (Kriest, 2002; Guidi et al., 2008a; Clements et al., 2023), provides a uniquely detailed perspective on the three-dimensional distribution of particulate organic carbon (POC) flux in the ocean (Guidi et al., 2016; Kiko et al., 2017; Cram et al., 2018).

Mesoscale eddies, as ubiquitous and energetic features in the global ocean, have been extensively studied for their roles in regulating physical dynamics, biogeochemical processes, and ecosystem structures (McGillicuddy Jr et al., 2016). Numerous studies have demonstrated that eddies can significantly influence nutrient transport, primary productivity, and biological community composition in the ocean (Stramma et al.,

2013; Zhang et al., 2020; Barone et al., 2022). Cyclonic eddies generally induce upwelling that brings cold,
80 nutrient-rich subsurface water into the euphotic zone, thereby stimulating new production and enhancing
phytoplankton biomass (Shih et al., 2020). This nutrient enrichment often favors the growth of large-sized
phytoplankton, particularly diatoms, leading to a community shift toward a more productive, herbivore-based
food web (Barlow et al., 2014; Wang et al., 2016). In contrast, anticyclonic eddies are typically characterized by
85 downwelling and enhanced water column stratification, which suppress vertical nutrient supply, leading to
reduced surface productivity and a food web dominated by smaller phytoplankton and microbial pathways
(Peterson et al., 2005; Stramma et al., 2013). Despite these advances, our understanding of how mesoscale
eddies influence the distribution and size structure of marine particles remains limited, particularly in marginal
seas. Key questions remain unanswered: To what extent do mesoscale eddies regulate particle abundance and
90 size composition? Do cyclonic and anticyclonic eddies exert distinct influence due to their contrasting physical
and biogeochemical characteristics? And critically, how do these differences in particle dynamics translate into
variability in vertical carbon export? The lack of observations and systematic analyses on these issues hampers
accurate assessments on biological pump efficiency in the ocean. Therefore, elucidating the impacts of
mesoscale eddies on particles characteristics, including abundance, size composition, and vertical transport
potential, is essential for improving our understanding of oceanic carbon cycling ~~and enhancing the reliability of~~
95 ~~biogeochemical models.~~

The South China Sea (SCS) is one of the largest semi-enclosed marginal seas, characterized by a narrow
and steep continental slope in its northern region (Zhang et al., 2020). This slope features a rapid bathymetric
gradient, with depths increasing sharply from less than 200 m at the shelf break to over 1000 m. Mesoscale
eddies are ubiquitous in the slope region of the SCS, where both cyclonic and anticyclonic eddies frequently
100 occur due to the combined influence of monsoonal winds, Kuroshio intrusion, and complex topography (Wu and
Chiang, 2007; Shih et al., 2020; Zhang et al., 2020). Typically spanning 100–200 km in diameter and persisting
for weeks to months, these eddies exhibit pronounced seasonal variability (Wu and Chiang, 2007). Cyclonic
eddies are more prevalent during the summer months, driven by enhanced upwelling and the southwesterly
monsoon, whereas anticyclonic eddies are more frequently observed in winter and early spring, often formed as
105 warm-core rings shed from the Kuroshio Current loop (Shih et al., 2020; Zhang et al., 2020). These eddies
propagate predominantly westward or southwestward along the northern continental slope of the SCS,
significantly modulating the vertical structure of temperature, salinity, and nutrient fields in this region (Guo et
al., 2015). While the impacts of mesoscale eddies on physical circulation, nutrient dynamics, and phytoplankton
community structures have been relatively well studied in this region (Wu and Chiang, 2007; Xiu and Chai,
110 2011; Wang et al., 2016; Xu et al., 2025), their influence on the distribution and size structure of marine
particles, especially in the context of carbon export processes, remains insufficiently explored. This lack of direct
observational constraints hinders our understanding of how marine particles regulate carbon export pathways and
respond to mesoscale physical processes.

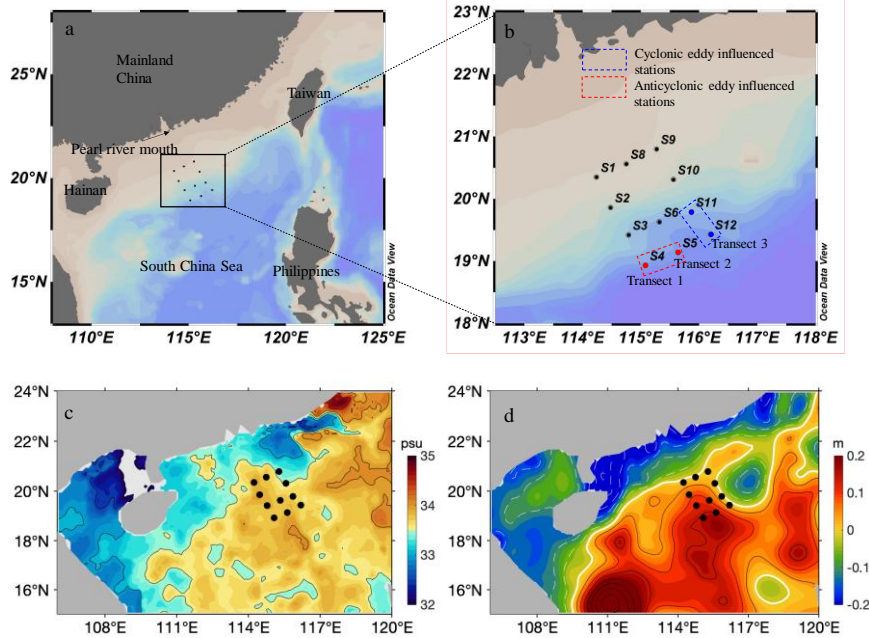
This study aims to fill the existing knowledge gaps by analyzing high-resolution UVP data collected along
115 the continental slope of the SCS during a 2015 cruise, during which a mesoscale anticyclonic-cyclonic eddy pair
was observed. Specifically, the objectives of this study are to (1) provide the first detailed characterization of the
spatial distribution of marine particles along the SCS slope and identify the key environmental factors driving
their variability, (2) analyze the size composition of particles and evaluate its implications for carbon cycling,
and (3) investigate the mechanisms by which mesoscale eddies modulate particles dynamics and their associated

120 POC fluxes. This study will elucidate the distribution patterns and controlling factors of marine particles along
the SCS slope, and provide new insights into how eddy-induced physical variability regulates particle dynamics
and their associated vertical transfer in the SCS.

2 Material and methods

125 2.1 Surveyed area and data acquisition

A research cruise was carried out in the SCS aboard the research vessel *Nanfeng* from June 13 to June 29,
2015. The study area and survey stations were shown in Fig. 1a. The survey stations can be divided into three
transects (Transect 1, Transect 2, and Transect 3) (Fig. 1b), which extend across the slope of the SCS, with
shallower sites at over 100 m and deeper sites exceeding 1000 m in depth (Table 1). Satellite data were used to
130 analyze the spatial and temporal variations in the physical and dynamic characteristics of the study region. The
Sea Surface Salinity (SSS) data consists of daily global, gap-free Level-4 (L4) analyses of SSS at a resolution of
1/8°. These analyses are generated through a multivariate optimal interpolation algorithm that combines SSS
data from different satellite sources, including NASA's Soil Moisture Active Passive (SMAP) and ESA's Soil
Moisture Ocean Salinity (SMOS) satellites, along with *in situ* salinity measurements provided by the Copernicus
135 Marine Environment Monitoring Service (Multi Observation Global Ocean Sea Surface Salinity and Sea Surface
Density) (Buongiorno Nardelli et al., 2016; Sammartino et al., 2022). Eddies were identified as local minima
(cyclonic eddies) and maxima (anticyclonic eddies) in sea level anomaly (SLA) using a composite altimetry
product, which is based on a combination of remote sensing observations distributed by the Copernicus Marine
Environment Monitoring Service (SEALEVEL_GLO_PHY_CLIMATE_L4_MY_008_057).



140 Fig. 1 Study area and survey stations in the SCS continental slope. a: the study region; b: the enlarge view; c: sea

surface salinity (SSS) at $1/8^\circ$ of resolution; d: sea level anomalies (SLA). The dots indicate the locations of the sampling stations. Red dots indicate stations influenced by the anticyclonic eddy, and blue dots represent stations located at the periphery of the cyclonic eddy.

145 Table 1. Location and deployment times of UVP5-HD in the study area. UVP deployment depth refers to the
 146 maximum depth reached during each profile. Sampled volume represents the total volume imaged by the
 147 UVP5-HD during each deployment. Station 7 was skipped due to instrument malfunction, and therefore not
 148 included in this study.

Station	Longitude (°E)	Latitude (°N)	Date	Time (hh:mm, UTC + 8)	Bottom depth (m)	UVP5-HD deployment depth (m)	Total particles ($\times 10^4$ #)	Sampled volume ($\times 10^3$ L)
S1	114.40	20.29	18- June- 2015	02:40 p.m.	123	110	101.74	5.99
S2	114.47	19.87	17- June- 2015	03:45 a.m.	587	500	182.55	12.80
S3	114.79	19.42	16- June- 2015	01:35 p.m.	1300	800	52.73	13.85
S4	115.08	18.93	15- June- 2015	11:45 p.m.	3000	800	64.79	15.39
S5	115.64	19.14	15- June- 2015	07:30 a.m.	2800	800	65.49	15.04
S6	115.32	19.63	14- June- 2015	03:25 p.m.	2108	800	66.24	15.77
S8	114.75	20.56	18- June- 2015	08:50 p.m.	120	100	95.83	6.47
S9	115.27	20.80	19- June- 2015	08:15 a.m.	170	110	49.97	7.28
S10	115.56	20.31	19- June- 2015	07:30 p.m.	560	500	69.98	5.84
S11	115.86	19.78	20- June- 2015	01:20 p.m.	1556	800	131.91	15.25
S12	116.20	19.43	21- June- 2015	01:45 p.m.	1971	800	51.39	5.64

149 Hydrographic measurements and water sampling were conducted using an SBE911 plus dual
150 conductivity-temperature-depth (CTD) sensor unit coupled with an SBE 32 Water Sampler (Seabird
151 Scientific, Bellevue, WA, USA). The CTD system recorded profiles of temperature (°C), salinity (psu),
152 and pressure (dbar) throughout the water column.

153 Nutrients and chlorophyll *a* (Chl *a*) concentrations were determined from seawater samples
154 collected at multiple depths using a 10 L Niskin sampler (KC-Denmark Inc., Denmark) deployed
155 alongside a CTD. For nutrient analysis, seawater samples were filtered through a 0.45 µm pore-size
156 cellulose acetate membrane, and the filtrates were stored at temperatures below -20 °C until further
157 processing. In the laboratory, nutrient concentrations were measured using a Technicon AA3
158 autoanalyzer (Bran-Luebbe GmbH) following standard protocols (Liu et al., 2022). The detection limits
159 for nutrient analysis were 0.02 µmol L⁻¹ for NO₃⁻, 0.01 µmol L⁻¹ for NO₂⁻, 0.03 µmol L⁻¹ for PO₄³⁻, and
160 0.05 µmol L⁻¹ for SiO₃²⁻. Chl *a* concentrations were determined using the fluorometric method
161 (Welschmeyer, 1994). Seawater samples (500 mL) were filtered through 0.7 µm Whatman GF/F filters,
162 and pigments were extracted in 90% acetone at 4 °C in the dark for 24 h. Fluorescence measurements
163 were then conducted using a Turner Designs fluorometer (Model 10).

164 2.2 Particle measurement

165 Particle size and abundance were measured using a high-resolution, high-frequency Underwater
166 Vision Profiler (UVP5-HD-5.0-HD). The UVP5-HD was mounted downward-facing on the CTD
167 Niskin-rosette, and vertical deployments were conducted at a descent speed of 1 m/s. The UVP5-HD
168 captured images of illuminated particles within a known sampling volume of 1.053 L per frame.

169 Particle size was determined based on the number of pixels in the captured images, ~~and the pixel-to-~~
170 ~~metric unit conversion followed the standard calibration procedures described by Picheral et al. (2010),~~
171 ~~which were established through laboratory experiments using natural particles in a seawater tank. Size-~~
172 ~~and volume calibrations were performed in a seawater tank using natural particles of various types to-~~
173 ~~establish the pixel to metric unit conversion (Picheral et al., 2010).~~ Images were recorded digitally at a
174 rate of 12 frames per second and processed using custom developed image analysis software ~~from the~~
175 ~~Laboratoire d'Océanologie de Villefranche-sur-Mer, including ZooProcess (v7.22) and PkID (v1.26).~~

176 The equivalent spherical diameter (ESD) of each particle was calculated under the assumption that the
177 particle's projected shape was circular. Particle volume concentration (PVC) was calculated by

带格式的: 字体: (默认) Times New Roman, 10 磅, 字
体颜色: 文字 1

178 summing the estimated volumes of all particles detected within each depth bin and normalizing by the
179 corresponding sampled water volume. The volume of each particle was estimated by assuming
180 spherical geometry based on the ESD. The final PVC is reported in $\text{mm}^3 \text{L}^{-1}$.

181 Previous inter-calibration studies of UVP systems have shown that only the overlapping size
182 ranges among different studies are suitable for comparative particle profile analyses (Guidi et al.,
183 2008a; Picheral et al., 2010). For consistency with previous studies, we set the upper size limit for
184 particle flux calculations at 1.5 mm ESD (Guidi et al., 2007, 2008a; Stemmann et al., 2008;
185 Ramondenc et al., 2016). The lower size limit was set at 100 μm ESD to exclude signals potentially
186 caused by camera resolution constraints and background noise, which could not be reliably
187 distinguished as actual particles (Fender et al., 2019). For data visualization in this study, particles were
188 categorized following Kiko et al. (2022) into two groups: small particles ($\text{ESD} < 0.50 \text{ mm}$) and large
189 particles ($\text{ESD} \geq 0.50 \text{ mm}$). This classification enables the examination of size-dependent vertical
190 distribution patterns, which can reflect underlying processes such as aggregation near the surface,
191 disaggregation at depth, and differential sinking behavior of particles of varying sizes.

192 To assess the influence of mesoscale eddies on the biological component of the particle field,
193 large particles were classified into living and non-living categories. In this context, living particles refer
194 specifically to large zooplankton, while all others were categorized as non-living particles. We
195 extracted and analyzed zooplankton data from the UVP5-HD imagery. Due to the resolution limitations
196 of the UVP5-HD, small particles could not be reliably imaged or morphologically classified in this
197 study. Vignette images of large particles were extracted from the UVP5-HD dataset and used for
198 zooplankton classification. The extracted images were uploaded to the EcoTaxa platform
199 (<https://ecotaxa.obs-vlfr.fr>), where a machine learning classifier (random forest algorithm) was applied
200 to assign objects into broad morphological categories, including zooplankton and non-living particles
201 (Picheral et al., 2017). All classified images were then visually checked and corrected by trained
202 analysts to ensure taxonomic accuracy. The abundance of zooplankton (ind. L^{-1}) was calculated by
203 dividing the number of individuals identified in each depth bin by the corresponding volume of water
204 imaged by the UVP5-HD.

205 **2.3 Estimation of POC export flux from particle size spectrum**

206 The POC export flux was estimated from particle size spectra using the method developed by

207 Guidi et al. (2008a, b). The particle size distribution (PSD) generally follows a power-law decrease
208 over the μm to mm size range (Guidi et al., 2009). This distribution, derived from UVP5-HD images, is
209 expressed as:

$$210 \quad n(d) = \alpha d^\beta \quad (1)$$

211 where d (mm) represents particles diameter, $n(d)$ is the particle size spectrum, α is normalization
212 constant and β is the exponent characterizing the slope of the number spectrum after log
213 transformation. The particle size-based carbon flux approach assumes that the total carbon flux, (F)
214 ($\text{mg C m}^{-2} \text{ d}^{-1}$), corresponds to the integral of the flux spectrum over all particle sizes, from the smallest
215 (d_{\min}) to the largest (d_{\max}) diameter:

$$216 \quad F = \int_{d_{\min}}^{d_{\max}} n(d) \cdot m(d) \cdot w(d) dd \quad (2)$$

217 where $n(d)$ is the particle number spectrum (particles $\text{m}^{-3} \text{ mm}^{-1}$), $m(d)$ (mg C) is the carbon mass of a
218 particle with diameter d , and $w(d)$ (m d^{-1}) is its sinking velocity.

219 The combined particle mass and settling velocity follow a power-law function of particle
220 diameter, based on empirical relationships derived from comparisons of PSDs obtained through
221 imaging systems and sediment trap mass flux estimates (Guidi et al., 2008a; Jouandet et al., 2011). This
222 relationship is expressed as: $m(d) \cdot w(d) = Ad^B$, where A (mg C m d^{-1}) and B are empirical constants. The
223 particle carbon flux can thus be approximated by discretizing Equation (2) into small logarithmic
224 diameter intervals (Guidi et al., 2009; Picheral et al., 2010):

$$225 \quad F = \sum_{i=1}^x n_i A d_i^B \Delta d_i \quad (3)$$

226 where $A = 12.5 \pm 3.40$ and $B = 3.81 \pm 0.70$, representing the best-fit parameters that minimized log-
227 transformed discrepancies between global oceanic sediment trap-derived carbon flux estimates and
228 UVP-derived particle abundance and PSDs (Guidi et al., 2008a). This approach has been widely
229 applied in various oceanic regions worldwide in recent years (Iversen et al., 2010; Ramondenc et al.,
230 2016; Fender et al., 2019; Clements et al., 2023; Wang et al., 2024a, b).

231 2.4 Data analysis

232 All particle size and abundance data obtained from the UVP5-HD were binned into 5 m vertical
233 intervals and subsequently processed to generate depth profiles of particle abundance (particles L^{-1}),
234 particle volume concentration ($\text{mm}^3 \text{ L}^{-1}$), and POC flux ($\text{mg C m}^{-2} \text{ d}^{-1}$). To visualize along-slope

235 variability, section plots were created for each transect by interpolating the se depth-resolved parameters
 236 particle abundance, volume concentration, and POC flux across stations. Statistical analyses were
 237 performed using SPSS 25.0. Two-tailed independent-sample *t*-tests were conducted to assess significant
 238 differences in particle and flux parameters between different depth layers and regions. Prior to applying
 239 *t*-tests, data normality and variance homogeneity were tested using the Shapiro-Wilk and Levene's tests,
 240 respectively (González-Estrada and Cosmes, 2019). For data not meeting parametric assumptions, non-
 241 parametric alternatives were used. Pearson correlation analysis was applied to evaluate the relationships
 242 between POC flux and environmental variables. Significance was defined at $p < 0.05$ unless otherwise
 243 stated. Hydrographic and particle data were visualized using Ocean Data View 4 and Origin 2022.

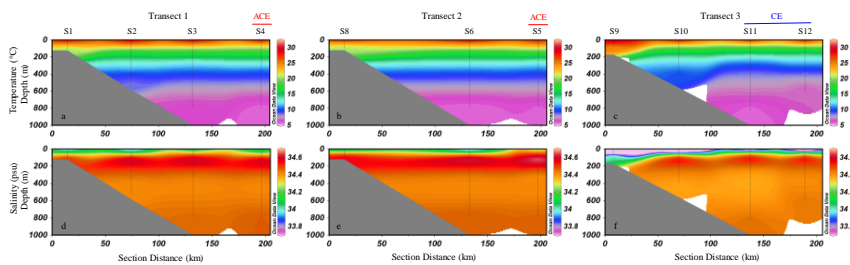
244

245 3 Results

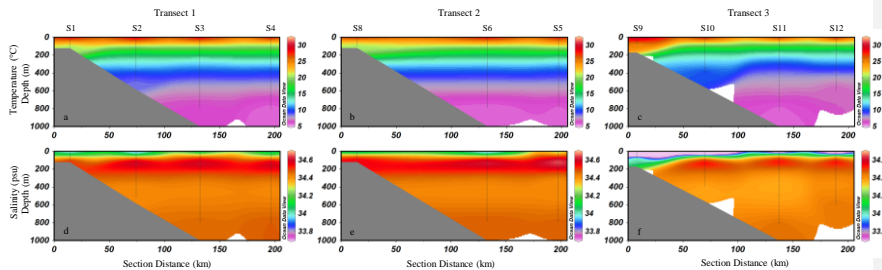
246 3.1 Hydrographic conditions

247 Based on the spatial distribution of SLA, two mesoscale eddies were present in the study area
 248 during the survey period: one cyclonic eddy and one anticyclonic eddy (Fig. 1d). Stations S4 and S5,
 249 located on the outer edge of Transects 1 and 2, respectively, were situated in a region where SLA
 250 exceeded +0.1 m, indicating influence from an anticyclonic eddy. In contrast, a distinct cyclonic eddy
 251 with SLA values below -0.1 m was present to the east of stations S11 and S12 in Transect 3. These two
 252 stations were positioned along the periphery of the cyclonic eddy, where the SLA gradient was steep.
 253 Vertically, the study area exhibits distinct characteristics of a tropical ocean, with relatively high sea
 254 surface temperature (~30 °C) and strong stratification in the upper 200 m (Fig. 2). A pronounced
 255 thermocline is observed between 100 and 200 m, marking a sharp temperature gradient (Fig. 2a-c).
 256 Salinity increases with depth, further reinforcing the stratification pattern (Fig. 2d-f).

257



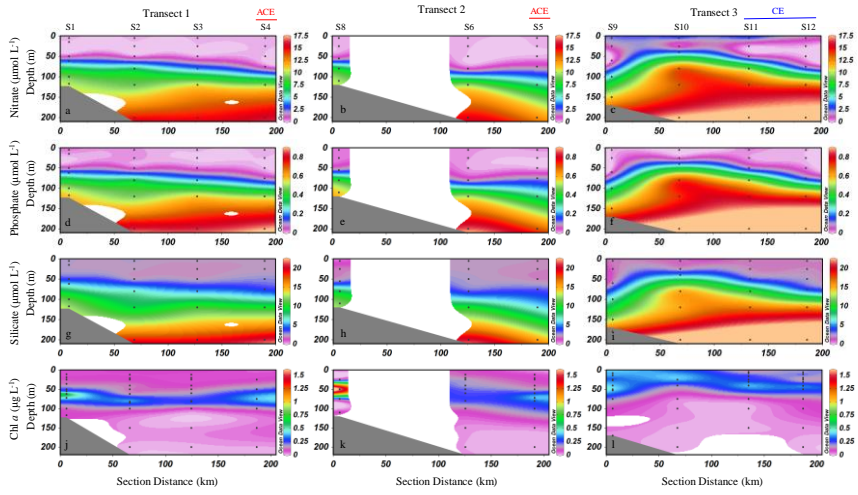
258



259

260 **Fig. 2. Vertical distribution of temperature (a-c, °C) and salinity (d-f, psu) along the three transects in the**
 261 **study area.**

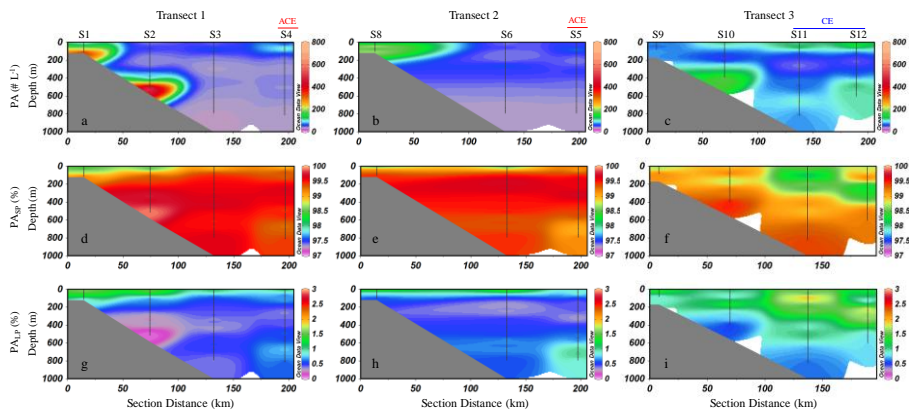
262 The sectional distributions of nutrients and Chl *a* concentrations in the study area are shown in Fig. 3.
 263 Nutrient profiles exhibit typical oligotrophic features, with low concentrations of nitrate, phosphate and
 264 silicate in surface waters and a pronounced nutricline between 50 and 100 m. Chl *a* exhibited a
 265 pronounced deep chlorophyll maximum, especially along Transect 1 and 2 (Fig. 3j, k). Along Transect
 266 3, the depth of the DCM became shallower, and Chl *a* concentrations were relatively high throughout the
 267 upper layer at nearshore stations (Fig. 3i). There were clear differences in the concentration of nutrients
 268 and Chl *a* between stations influenced by the anticyclonic eddy (S4, S5) and those influenced by the
 269 cyclonic eddy (S11, S12) (Supplementary Fig. S1). Nutrient concentrations at stations S11 and S12 were
 270 generally higher than those at stations S4 and S5 from 0 to 200 m (Supplementary Fig. S1a-c). Chl *a*
 271 concentrations were higher at stations S11 and S12 than at stations S4 and S5 in the upper 50 m layer
 272 (Supplementary Fig. S1d). With increasing depth, Chl *a* levels at S11 and S12 gradually declined,
 273 whereas those at S4 and S5 continued to rise, peaking at approximately 75 m before decreasing again.



274
 275 **Fig. 3.** Sectional distribution of nutrient concentrations (nitrate, phosphate, and silicate) ($\mu\text{mol L}^{-1}$) and Chl
 276 ***a*** concentrations ($\mu\text{g L}^{-1}$) in the upper 200 m of the study area. a-c: nitrate ($\mu\text{mol L}^{-1}$); d-f: phosphate (μmol
 277 L^{-1}); g-i: silicate ($\mu\text{mol L}^{-1}$); j-l: Chl *a* ($\mu\text{g L}^{-1}$). ACE denotes stations influenced by the anticyclonic eddy,
 278 while CE denotes stations influenced by the cyclonic eddy.

279 **3.2 Particle concentration and size structure**

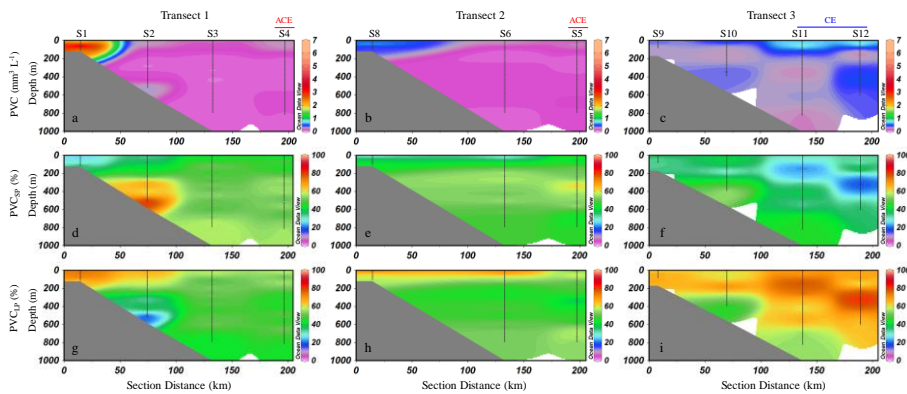
280 Particle abundances ranged from 0 to 783 particles L⁻¹, with a mean of 68 ± 68 particles L⁻¹ (mean ± SD). The
 281 vertical profiles of particle abundance across the three transects were shown in Fig. 4. In Transect 1, high particle
 282 abundance was observed at station S1 and the bottom layer of station S2, with values reaching up to 700 particles
 283 L⁻¹ (Fig. 4a). In Transect 2, particle abundance gradually decreased from the inner shelf to the outer slope and from
 284 surface to bottom waters (Fig. 4b). In Transect 3, a distinct peak in particle abundance was observed at 379–390
 285 m depth at the slope station S10 (Fig. 4c). Furthermore, at the outermost stations S11 and S12, elevated particle
 286 concentrations were observed in the upper 50 m of the water column, with peak values reaching up to 200 particles
 287 L⁻¹. This is notably higher than the maximum particle abundances recorded at stations S4 and S5, where values
 288 remained below 150 particles L⁻¹ (Fig. 4a, b). The distribution patterns of zooplankton (Supplementary Fig. S2) in
 289 the study area were generally similar with that of particle abundances. On transects 1 and 2, higher zooplankton
 290 abundances were observed at the nearshore stations, with a decreasing trend toward offshore stations
 291 (Supplementary Fig. S2a, b). In contrast, on transect 3, elevated abundances were recorded at the outer stations
 292 S11 and S12 (Supplementary Fig. S2c). Regarding particle size composition, small particles overwhelmingly
 293 dominated the total particle abundance, consistently accounting for more than 97% across all transects and
 294 throughout the water column (Fig. 4d-f). In contrast, large particles contributed only a minor fraction of the total
 295 abundance at all depths and locations (Fig. 4g-i).



296
 297 **Fig. 4 Vertical distribution of particles abundance (PA, # L⁻¹) and the relative proportion of small particles (PA_{SP}, ESD**
 298 **< 500 μm) and large particles (PA_{LP}, ESD ≥ 500 μm) within the total particle abundance. PA: a-c; PA_{SP}%; d-f;**
 299 **PA_{LP}%; g-i. SP: small particles; LP: large particles. ACE represents stations influenced by anticyclonic eddies, while**
 300 **CE represents stations influenced by cyclonic eddies. Interpolated values between S6 and S8 are automatically**
 301 **generated by ODV and should be interpreted with caution.**
 302 **the relative proportion of small particles (ESD < 500 μm) and large particles (ESD ≥ 500 μm) within the total particle**
 303 **abundance.**

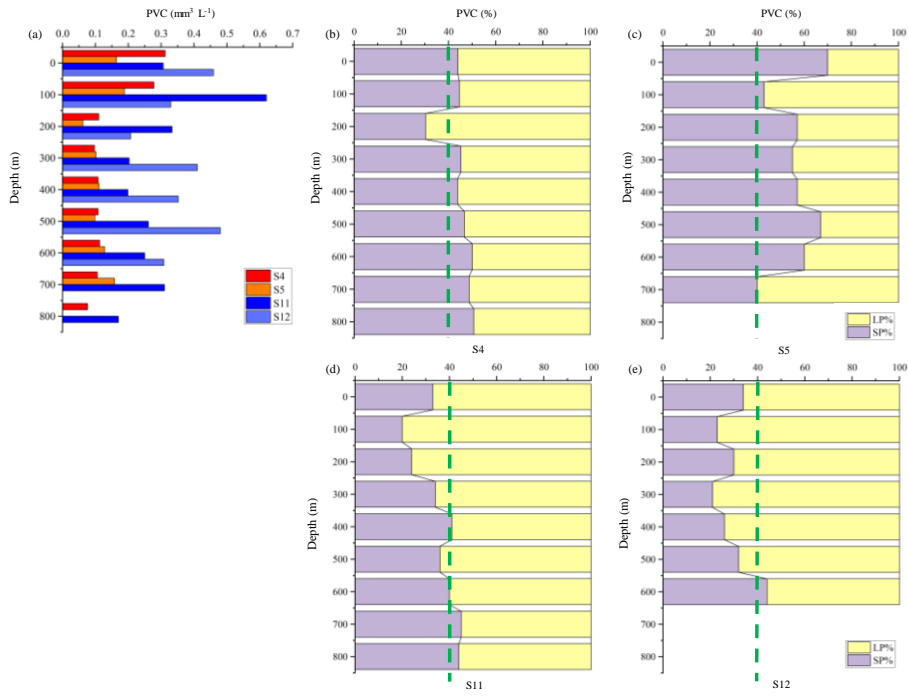
304 The distribution of PVC along the three transects, as well as the proportions of small and large particles
 305 contributing to PVC, are shown in Fig. 5. PVC ranged from 0 to 6.7 mm³ L⁻¹, with a mean of 0.3 ± 0.4 mm³ L⁻¹
 306 (mean ± SD) in this study. Overall, high PVC values in the study area were primarily observed in the upper water
 307 column, while values decreased markedly as water depth increased (Fig. 5a-c). In waters shallower than 200 m,
 308 the mean PVC was 0.4 ± 0.7 mm³ L⁻¹ (mean ± SD), which was significantly higher than that in waters deeper than

309 200 m, where the mean PVC was $0.2 \pm 0.1 \text{ mm}^3 \text{ L}^{-1}$ (mean \pm SD) (t -test, $p < 0.01$). In Transect 1, PVC was highest
 310 at the inner slope station S1 and progressively decreased toward the outer slope stations (Fig. 5a). A similar pattern
 311 was observed in Transect 2, where PVC was elevated at the inner slope station S8, followed by a gradual decline
 312 toward the outer slope (Fig. 5b). In Transect 3, PVC was relatively high in upper layers at the outermost stations
 313 S11 and S12, with concentrations decreasing with depth (Fig. 5c). For the whole study region, small particles
 314 contribute between 13% and 74% (mean \pm SD: $39\% \pm 12\%$) of the total PVC (Fig. 5d-f), while large particles
 315 account for 26% to 87% (mean \pm SD: $61\% \pm 12\%$) (Fig. 5g-i). For small particles, their contribution to PVC was
 316 generally around 40%–50% across most areas (Fig. 5d-f). However, notable variations were observed in certain
 317 regions. At station S2, a sharp increase occurred in the bottom layer, where the proportion exceeded 60% (Fig. 5d).
 318 In contrast, at stations S11 and S12, a marked decrease was observed in the upper to mid-depth layers, where the
 319 proportion dropped to 30% or even lower (Fig. 5f).



320
 321 **Fig. 5. Distribution of particle volume concentration (PVC) ($\text{mm}^3 \text{ L}^{-1}$) along the three transects and the percentage**
 322 **contributions of small and large particles. PVC: a-c; percentage of small particles: d-f; percentage of large particles:**
 323 **g-i. SP: small particles; LP: large particles. ACE represents stations influenced by anticyclonic eddies, while CE**
 324 **represents stations influenced by cyclonic eddies. Interpolated values between S6 and S8 are automatically generated**
 325 **by ODV and should be interpreted with caution.**

326 Figure 6 shows the PVC values at different depths and the percentage contributions of small and large
 327 particles at stations influenced by anticyclonic eddies (S4, S5) and cyclonic eddies (S11, S12). Notable differences
 328 in PVC values and particle size composition can be observed between these two regions. At nearly all depth, PVC
 329 at S11 and S12 is higher than at S4 and S5 (Fig. 6a). At S4 and S5, small particles generally contribute more than
 330 40% to PVC across most all depths, except at 200 m at S4, whereas while large particles remain below contribute
 331 less than 60% (Fig. 6b, c). In contrast, at S11 and S12, the proportion contribution of small particles is
 332 mostly generally below less than 40% at most depths, especially particularly above 500 m, with whereas large
 333 particles contributing the majority of the volume more than 60% (Fig. 6d, e). The proportion of large particles at
 334 S11 and S12 is higher than at S4 and S5.



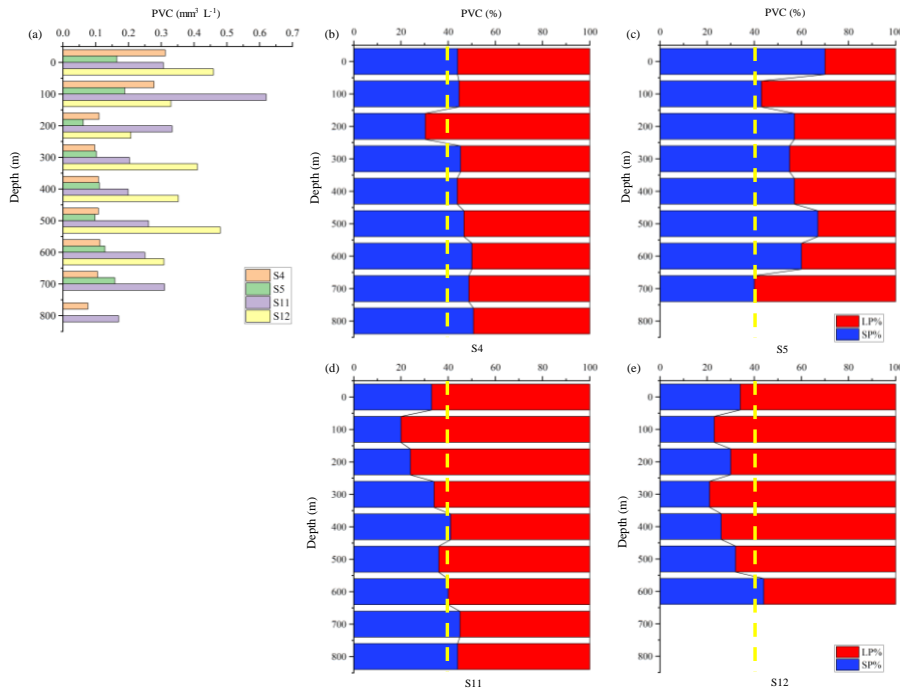


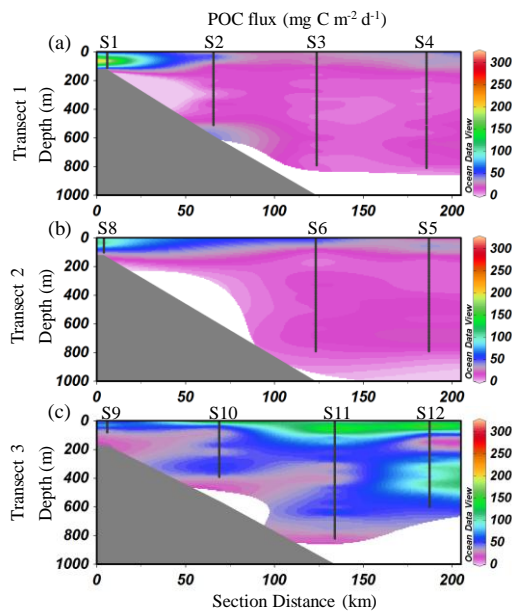
Fig. 6. PVC ($\text{mm}^3 \text{L}^{-1}$) at different depths at stations influenced by anticyclonic eddies (S4, S5) and cyclonic eddies (S11, S12) and the contributions of small particles and large particles.– a: PVC at each layer; b-e: size composition of PVC at each station. SP: small particles; LP: large particles. The green dashed line represents a 40% reference threshold to visually distinguish the dominant size class. This threshold is not based on statistical testing but serves as a comparative guide.

3.3 POC export flux and spatial variability

The POC export flux, derived from UVP-based particle size distributions, exhibited a wide range from 3.4 to 302.4 $\text{mg C m}^{-2} \text{d}^{-1}$, with a mean value of $33.6 \pm 34.9 \text{ mg C m}^{-2} \text{d}^{-1}$ across the study area. Overall, high POC fluxes were primarily concentrated in the upper 200 m (Fig. 7). In Transect 1, the highest fluxes were concentrated at the nearshore station S1, particularly within the 50–70 m depth range, where values peaked at 302.0 $\text{mg C m}^{-2} \text{d}^{-1}$ (Fig. 7a). In contrast, offshore stations along the same transect displayed significantly lower fluxes, generally below 40 $\text{mg C m}^{-2} \text{d}^{-1}$. A similar nearshore-to-offshore gradient was observed in Transect 2, where the maximum flux (164.0 $\text{mg C m}^{-2} \text{d}^{-1}$) was recorded at 40 m depth at station S8, gradually decreasing toward deeper slope stations (Fig. 7b). Transect 3 showed a distinct pattern, with elevated POC fluxes occurring at offshore stations S11 and S12 (Fig. 7c). At station S11, the highest flux (212 $\text{mg C m}^{-2} \text{d}^{-1}$) was recorded at 60 m, while at station S12, the flux peaked at 210 $\text{mg C m}^{-2} \text{d}^{-1}$ at 40 m.

The contribution of small and large particles to POC flux across the study area was shown in Supplementary Fig. S3. Small particle-derived carbon flux accounted for 5% to 77% of the total POC flux, with an average contribution of $24\% \pm 12\%$, while large particle-derived carbon flux ranged from 23% to 95%, averaging $76\% \pm$

12%. The contribution of large particles to the POC flux was significantly higher than that of small particles (t -test, $p < 0.05$). Vertically, in waters shallower than 200 m, small particles contributed $19 \pm 9\%$ (mean \pm SD) to the POC flux, while large particles accounted for $81 \pm 9\%$ (mean \pm SD). In contrast, below 200 m, the contribution of small particles increased to $28 \pm 12\%$ (mean \pm SD), with large particles contributing $72 \pm 12\%$ (mean \pm SD). The contribution of small particles to POC flux below 200 m was significantly higher than that in the upper 200 m (t -test, $p < 0.05$).



365 **Fig. 7 Vertical distribution of POC flux across the three transects ($\text{mg C m}^{-2} \text{d}^{-1}$) in the study area. a: Transect 1; b:**
Transect 2; c: Transect 3. Interpolated values between S6 and S8 are automatically generated by ODV and should be
interpreted with caution.

370 The POC flux patterns differed markedly between stations influenced by anticyclonic eddies (S4, S5) and cyclonic eddies (S11, S12) (Fig. 8). In terms of flux magnitude, the highest values at all stations were observed above 100 m. However, POC fluxes at S11 and S12 were consistently higher than those at S4 and S5 across all depths (Fig. 8a). Regarding flux composition, the contribution of small particles to the POC flux was generally higher at the anticyclonic eddy-influenced stations S4 and S5 than at the cyclonic eddy-influenced stations S11 and S12 (Fig. 8b), whereas the contribution of large particles was greater at S11 and S12 compared to S4 and S5 (Fig. 8c).

375

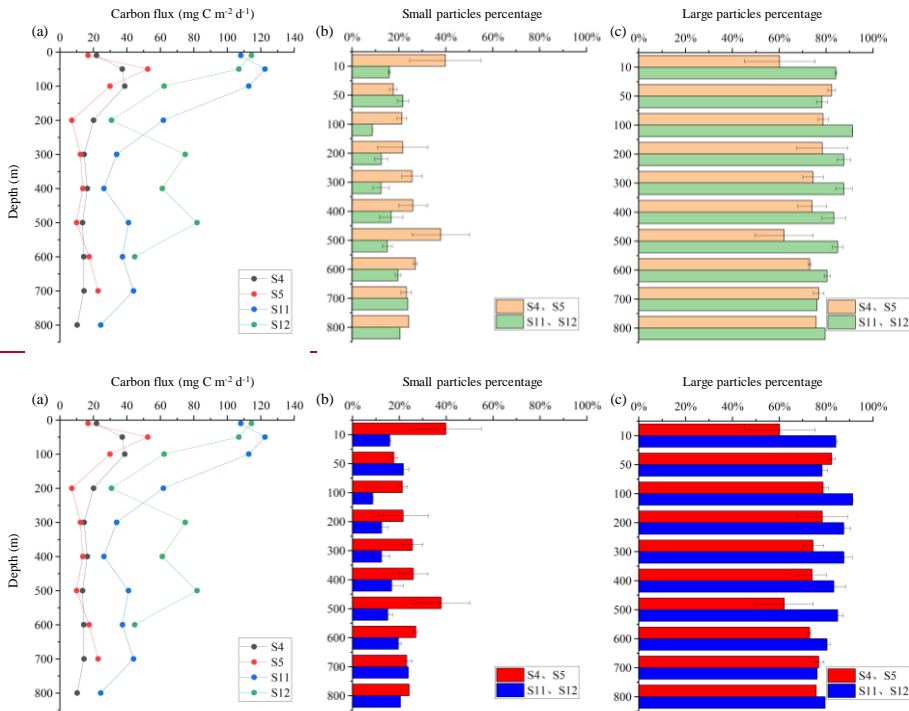
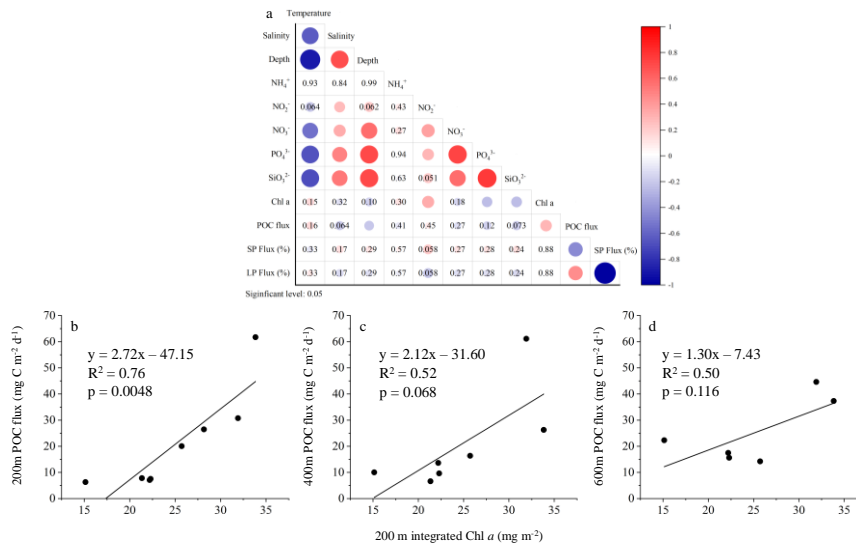


Fig. 8 POC flux derived from UVP5-HD data in different water layers and contributions of small and large particles in the anticyclonic eddy region (S4, S5) and cyclonic eddy region (S11, S12). a: Carbon flux ($\text{mg C m}^{-2} \text{d}^{-1}$); b: Small particles percentage; c: Large particles percentage. b, c: mean values and standard deviations of those two stations.

380

381 The results of the Pearson correlation analysis indicate that POC flux does not exhibit significant correlations
 382 with most environmental factors in the upper 200 m layer, except for water depth and Chl *a* concentration (Fig.
 383 9a). POC flux shows a significant negative correlation with water depth and a significant positive correlation with
 384 Chl *a* concentration. Scatter plot analyses further revealed significant positive relationships between POC flux at
 385 200 m and the water-column integrated Chl *a* concentrations above 200 m (Fig. 9b). For the 400 m and 600 m
 386 depth layers, the POC flux showed no significant correlation with the integrated Chl *a* concentration in the upper
 387 200m of the water column (Fig. 9c, d).



388 **Fig. 9** Correlation analysis between POC flux and environmental factors.

389 **a:** Heatmap showing Pearson correlation coefficients (r) between POC flux and environmental variables in the
 390 upper 200 m. Significant correlations ($p < 0.05$) are highlighted by filled circles with color intensity proportional to r ,
 391 but the correlation coefficient values are not labeled. Non-significant correlations ($p \geq 0.05$) are indicated by numeric r
 392 values only. **b-d:** Correlation between POC ($\text{mg C m}^{-2} \text{d}^{-1}$) flux at 200 m, 400 m, and 600 m depth and the integrated
 393 Chl *a* concentration (mg m^{-2}) in the upper 200m. SP: small particle; LP: large particle. A significance level of $p < 0.05$
 394 was used to determine statistical significance.

4 Discussion

4.1 Marine particle distribution and controls: cross-system comparisons and regional characteristics

400 The particle abundance and PVC observed with UVP5-HD along the SCS slope in this study offer important
 context for understanding regional particle dynamics. When compared to UVP data from other oligotrophic
 oceanic regions, our findings fall within the broad range of particle concentrations and volume reported for similar
 low-nutrient systems (Table 2). This comparison also highlights the role of environmental variability in shaping
 particle distributions in the oligotrophic SCS. The particle abundance in the SCS continental slope (0–100 m: 25–
 476 particles L^{-1} ; 0–800 m: 0–783 particles L^{-1}) is comparable to values reported for other oligotrophic regions
 405 such as the High Nutrient, Low Chlorophyll (HNLC) areas of the Southern Ocean (0–100 m: 0–500 particles L^{-1} ;
 Jouandet et al., 2011), and markedly higher than those observed in the mesopelagic zone (200–1000 m) of the

equatorial Pacific (1–4 particles L⁻¹; Pretty, 2019). However, it is notably lower than the particle abundance during an iron-fertilized bloom station in the Southern Ocean (1400 ± 200 particles L⁻¹; Jouandet et al., 2011), where artificial nutrient enrichment significantly boosted particle production. This discrepancy underscores the influence of localized biogeochemical conditions on particle abundance. In terms of particle volume concentration (PVC), the SCS slope exhibits values ranging from 0–6.7 mm³ L⁻¹ (mean ± SD: 0.3 ± 0.4 mm³ L⁻¹), aligning well with the Gulf of Alaska shelf (0.1–1 mm³ L⁻¹; Turner et al., 2017) and the HNLC stations in the Southern Ocean (0–50 mm³ L⁻¹; Jouandet et al., 2011). Conversely, these values are lower compared to the iron-fertilized bloom stations in the Southern Ocean (183 ± 34 mm³ L⁻¹; Jouandet et al., 2011), reflecting the significant impact of primary production and aggregation processes. The differences between regions suggest the importance of local environmental factors, including nutrient availability and primary production, in shaping marine particle dynamics.

417 **Table 2 Comparison of particle abundances and volume concentrations in this study with those in other studies. —:**
 418 **no data. Data from the upper 100 m layer are presented separately to facilitate comparison with previous studies**
 419 **using similar sampling depths (e.g. Iversen et al., 2010; Jouandet et al., 2011).**

Location	Depth (m)	Particle abundance range (mean \pm SD) (L ⁻¹)	PVC range (mean \pm SD) (mm ³ L ⁻¹)	Reference
The North Mediterranean	0–400	0–80	—	Gorsky et al., 2000
The Ligurian Sea	0–1000	0–1108	—	Stemmann et al., 2008
Off Cape Blanc, NW Africa	0–80	30–100	—	Iversen et al., 2010
The HNLC stations in the Southern Ocean	0–100	0–500	0–50	Jouandet et al., 2011
Iron-fertilized bloom station in the Southern Ocean	0–100	1400 \pm 200	183 \pm 34	Jouandet et al., 2011
Southeast of Kerguelen Island (Southern Ocean)	0–100	90 \pm 5	0.3 \pm 0.1	Jouandet et al., 2014
The Gulf of Alaska shelf	0–40	—	0.1–1	Turner et al., 2017
The Equatorial Pacific	200–1000	1–4	—	Pretty, 2019
The North Pacific Gyre	>1000	0.1–0.3	—	Pretty, 2019
The eastern tropical North Pacific	160–500	1–10	—	Cram et al., 2022
Station ALOHA (22.75°N, 158.00°W)	0–75	50–125	—	James, 2024
SCS slope	0–100	25–476 (95 \pm 71)	0.0–6.7 (0.6 \pm 0.8)	This study
SCS slope	0–800	0–783 (68 \pm 69)	0.0–6.7 (0.3 \pm 0.4)	This study

420

Horizontally, particle abundance and PVC exhibited clear cross-shelf gradients, with higher values observed at the inner slope stations, and a decreasing trend toward offshore waters (Fig. 4a-c; Fig. 5a-c). This pattern is consistent with observations from several other oceanic regions. Guidi et al. (2008b) studied the distribution of particles ($>100 \mu\text{m}$) in the South-Eastern Pacific, and found that particle concentrations were highest over the
425 Peru-Chile continental shelf, and decreased progressively toward the open ocean. Forest et al. (2012) found that particle abundance and volume in the surface layer of southeast Beauford Sea exhibited a decline of approximately two orders of magnitude when progressing from the shelf toward the basin. Turner et al. (2017) measured the concentrations of marine particles in the Gulf of Alaska during summer 2015, and found that particle concentrations were highest at stations closest to large inputs of freshwater and glacial discharge, intermediate at
430 some nearshore stations, and lowest over the mid-shelf. Therefore, our results, in line with previous studies, indicate that particle concentrations tend to be higher in nearshore regions. In this study, it was observed that the depth of the nutricline at inner slope stations was shallower than that at outer slope stations (Fig. 3). The shallow nutricline observed at inner slope stations could enhance light availability in the SCM layer, likely promoting higher Chl *a* concentrations. The distribution of Chl *a* also clearly indicates that the DCM layer at inner slope
435 stations exhibited higher Chl *a* concentrations compared to outer slope stations (Fig. 3j-l). The resulting increase in phytoplankton biomass may stimulate organic matter production and particle aggregation (Panaïotis et al., 2024), thereby contributing to elevated particle concentrations there. Additionally, nearshore regions are more susceptible to terrestrial inputs. On one hand, terrestrial input can supply nutrients, stimulating primary productivity and particle formation (Turner et al., 2017). On the other hand, the proximity to the continental margin increases
440 exposure to lithogenic inputs from terrestrial sources (Liu et al., 2016), further enhancing particle loads in inner slope waters. Therefore, from a horizontal perspective, the combined influence of terrestrial inputs and a shallower nutricline in inner shelf regions enhances biogeochemical processes that lead to higher particle concentrations there.

In addition to identifying patterns of particle distribution that are consistent with observations from other
445 oceanic regions, we also observed several localized and unique features specific to this region. The most notable one is the elevated particle abundances and PVC observed at stations S11 and S12 (Fig. 4c, Fig. 5c). At stations S11 and S12, surface particle abundance and PVC reached as high as $130 \text{ particles L}^{-1}$ and $0.45 \text{ mm}^3 \text{ L}^{-1}$, respectively, substantially higher than those observed at the inner slope station S9, which recorded $80 \text{ particles L}^{-1}$ and $0.18 \text{ mm}^3 \text{ L}^{-1}$. Given their offshore location ($> 200 \text{ km}$ from land), the particle enrichment at these sites is
450 unlikely to stem from terrestrial inputs and instead reflects localized biological production. Mesoscale eddies are known to influence upper-ocean nutrient supply, productivity levels, and the physical structure of the water column (Maiti et al., 2008). Cyclonic eddies, in particular, induce upward vertical transport that enhances nutrient supply to the euphotic zone, stimulating phytoplankton growth and aggregate formation (Kahru et al., 2007). Furthermore, convergence and retention zones along the eddy periphery can trap suspended and sinking particles, facilitating
455 localized particle accumulation (Accardo et al., 2025). In our study, the elevated particle concentrations at S11 and S12 support this mechanism, suggesting a coupling between eddy-driven nutrient enhancement and biological particle production. Another localized and distinct observation was the exceptionally high particle abundance detected in the bottom layers at stations S2 and S10 (Fig. 4a, c). At the bottom layer at these two stations, the particle population was overwhelmingly dominated by small particles, which accounted for more than 99.8% of
460 the total abundance (Fig. 4d, f). This explains why the exceptionally high particle numbers did not correspond to elevated PVC values there. Given the low particle concentrations observed in the upper water column at these two

stations, it is unlikely that the elevated particle abundance in the bottom layer resulted from vertical settling from above. ~~However, the low abundance of large zooplankton observed in this area (Supplementary Fig. S2a, c) does not support the presence of substantial amount of living particles in the bottom layer.~~ One plausible explanation for this deep particle enrichment is the presence of intermediate nepheloid layers (INLs). INLs are formed by suspended particles spreading along isopycnal surfaces and are commonly found near the edges of continental shelves, slopes, and seamounts (Oliveira et al., 2002). In the SCS, they are primarily formed as a result of resuspension and lateral transport of fine particles along the continental slope (Jia et al., 2019; Chen et al., 2024). The composition of INLs typically consists of a mixture of fine-grained lithogenic particles, resuspended sediments, and biogenic detritus (Oliveira et al., 2002). ~~In this study, small particles could not be imaged, and thus their composition remains unknown.~~ However, the low abundance of large zooplankton observed in this area (Supplementary Fig. S2a, c) does not support the presence of substantial amount of living particles in the bottom layer. The exceptionally high particle abundance observed here is more likely derived from sediment resuspension rather than from vertical export originating in the euphotic layer. ~~In contrast, a different case was observed at station S4. A slight elevation in particle abundance was found in the upper 100 m (Fig. 4a), and image analysis confirmed that this layer was also associated with an elevated concentration of large zooplankton (Supplementary Fig. S2a). Given that this station was sampled during nighttime (Table 1), it is plausible that this particle peak resulted from diel vertical migration, during which zooplankton ascend toward the surface at night and contribute to increased particle signal via biological presence and pellet production (Hays, 2003). This observation suggests that in addition to physical processes such as eddy dynamics and lateral resuspension, vertical migratory behavior of zooplankton may also modulate fine-scale particle distributions.~~

4.2 Numerical dominance of small particles vs. biogeochemical significance of large particles

The size composition of marine particles is critically important, as it governs their sinking efficiency, with smaller particles typically sinking much more slowly than larger ones (Clements et al., 2023). In addition, vertical variations in particle size composition can offer insights into particle degradation and transformation processes occurring within the water column (Cram et al., 2022). Using data from the UVP5-HD, this study characterizes the size composition of marine particles along the SCS slope. Small particles contributed over 98% to the total particle abundance in most areas (Fig. 4d-f), highlighting their overwhelming numerical dominance. Slight decreases in the relative contribution of small particles were only observed in certain high-productivity regions, such as the nearshore stations of Transects 1 and 2, and stations S11 and S12 along Transect 3. Due to the lack of image data for small particles, we were unable to determine the exact cause of the decreased proportion of small particles in these areas. The study area represents a typically oligotrophic environment. Previous studies have reported low phytoplankton productivity in this region, with the community largely dominated by picophytoplankton (Zhang et al., 2023). The low biomass and small size of phytoplankton cells limit their ability to form large particles or aggregates through aggregation processes. Additionally, low primary productivity is often accompanied by low zooplankton abundance (Liu et al., 2020). The low biomass of large-sized zooplankton further limits the production of large particles, contributing to the dominance of small particles in abundance.

Although small particles overwhelmingly dominated in terms of abundance, the pattern was notably different when PVC was considered. Across the entire study area, small particles contributed between 13% and 74% of the total PVC (mean \pm SD: 39% \pm 12%) (Fig. 5d-f), whereas large particles accounted for a substantially higher share, ranging from 26% to 87% (mean \pm SD: 61% \pm 12%) (Fig. 5g-i). This contrast became even more pronounced when examining carbon fluxes. Small particle-derived POC flux accounted for 5% to 77% of the total, with an

average contribution of $24\% \pm 12\%$, whereas large particles contributed the majority of carbon export, ranging from 23% to 95%, with a mean of $76\% \pm 12\%$ (Supplementary Fig. S3). This apparent disconnect between numerical dominance and carbon export efficiency underscores the importance of particle size in determining vertical carbon flux (Cram et al., 2018). Smaller particles tend to have lower sinking velocities due to their higher surface-area-to-volume ratios and reduced mass, which makes them more susceptible to microbial degradation, grazing, and disaggregation in the upper ocean (Riley et al., 2012; Durkin et al., 2015). In contrast, large particles—such as fast-sinking marine snow aggregates, fecal pellets, and large phytoplankton or zooplankton carcasses—settle more rapidly and are therefore more efficient vehicles for transporting organic carbon to depth (Iversen et al., 2010; Forest et al., 2012). In our study, the dominance of small particles in abundance but their relatively minor role in POC flux suggests that carbon export efficiency in the SCS slope region is largely regulated by the production and fate of large, fast-sinking particles.

The vertical partitioning of POC flux between small particles and large particles also revealed distinct depth-dependent patterns. In the upper 200 m, small particles contributed an average of $19\% \pm 9\%$ to the total POC flux, while large particles dominated with $81\% \pm 9\%$. Below 200 m, the relative contribution of small particles increased to $28\% \pm 12\%$, whereas that of large particles declined to $72\% \pm 12\%$. The enhanced contribution of small particles at depth was statistically significant (t-test, $p < 0.05$). This trend suggests that, although large particles dominate carbon export in the upper ocean, small particles become increasingly important in the mesopelagic zone. Several mechanisms may account for this shift. Large particles, such as fecal pellets and marine snow aggregates, typically sink rapidly and can reach depth with relatively little degradation (Turner, 2015). However, they are also more prone to fragmentation and microbial decomposition during descent, especially in the upper mesopelagic zone (Stamieszkin et al., 2017). As these large particles disaggregate, they contribute to the pool of smaller, slower-sinking particles, thereby increasing the relative contribution of small particles to the total flux at greater depths. In contrast, small particles—although less efficient in transporting carbon due to their slower sinking velocities and higher residence times—can persist longer in the water column. On the other hand, as discussed in Section 4.1, nepheloid layers were observed in the bottom waters along the SCS slope. This process can introduce substantial amounts of fine sediment particles into the water column through resuspension and lateral transport (Zhou et al., 2020; Chen et al., 2024), further contributing to the increased proportion of small particles in the mesopelagic POC flux. Therefore, the elevated contribution of small particles to POC flux in the mesopelagic layer may reflect not only the progressive disaggregation of larger particles during sinking, but also the influence of resuspended fine sediments associated with nepheloid layers. These observations highlight the dynamic nature of particle flux attenuation and transformation with depth in this region.

4.3 Eddy-driven variability in particle dynamics and carbon export

Mesoscale eddies are highly frequent in the SCS, with 230 eddies generated on average each year (Jin et al., 2024). These eddies exert a profound influence on regional biogeochemical processes (Xiu and Chai, 2011; Guo et al., 2015; Xu et al., 2025). Accounting for their impact is essential when examining particle characteristics and carbon export in this dynamic region. In this study, we compared particle characteristics between two contrasting eddy regimes: a cyclonic eddy (stations S11 and S12) and an anticyclonic eddy (stations S4 and S5). Across most of the water column (0–800 m), PVC was markedly higher in the cyclonic eddy region than in the anticyclonic region (Fig. 6a). This pattern likely reflects the enhanced nutrient availability and elevated phytoplankton biomass observed under cyclonic eddy influence, which favored the formation of biogenic particles.

带格式的: 字体: Times New Roman

545 regimes were encountered: an anticyclonic eddy influencing stations S4 and S5, and a cyclonic eddy encompassing
the periphery of stations S11 and S12 (Fig. 1d). The comparison between cyclonic and anticyclonic eddy stations
revealed distinct differences in vertical nutrients distribution. At the cyclonic eddy stations (S11 and S12), nutrient
concentrations in the upper 200 m, particularly between 50 and 200 m depth, were significantly elevated compared
to those at the anticyclonic eddy stations (S4 and S5) (Supplementary Fig. S1a-c, *t*-test, $p < 0.01$). This nutrient
enrichment likely resulted from upwelling processes induced by the cyclonic eddy, which supplied subsurface
nutrients to the euphotic zone (Guidi et al., 2012; Zhou et al., 2021). Several studies have documented similar
550 processes in the SCS, where cyclonic eddies promote the upward transport of nutrients from the subsurface, while
anticyclonic eddies have the opposite effect, deepening the nutricline and resulting in nutrient depletion in the
upper water column (Shih et al., 2020; Xu et al., 2025). Consequently, phytoplankton biomass, reflected by Chl *a*
concentrations, responded to these changes in vertical nutrient distribution. Notably, Chl *a* concentrations in the
upper water column were substantially higher at station S11 and S12 compared to S4 and S5 (Supplementary Fig.
555 S1d). The integrated Chl *a* concentrations above 75 m were 14.34 and 19.18 mg m⁻² at S11 and S12, respectively,
exceeding the values observed at S4 (13.95 mg m⁻²) and S5 (9.19 mg m⁻²). These results suggest that under
influence of the cyclonic eddy, phytoplankton production in the upper water column at S11 and S12 was enhanced
relative to the anticyclonic eddy-affected stations S4 and S5. Accordingly, PVC at stations S11 and S12 was
significantly higher than that at stations S4 and S5 throughout most of the water column from the surface to 800
560 m (Fig. 6a).

In addition to PVC, the two eddy type regions also exhibited distinct particle size structures patterns in
the size composition of PVC (Fig. 6b-c). In the anticyclonic eddy region at stations S4 and S5, small particles
generally contributed accounted for more than 40% of the total PVC throughout the water column, with average
contributions of 45% ± 6% (mean ± SD) at station S4 and 55% ± 10% (mean ± SD) at station S5, respectively. In
565 the cyclonic eddy region, contrast, the proportion of small particles was noticeably lower, with average contributions
of at stations S11 and S12 was noticeably lower, averaging 35% ± 8% at station S11 (mean ± SD) and 30% ± 7%
at station S12 (mean ± SD), respectively, and typically remaining below 40% throughout the water column. This
contrast indicates that the two types of mesoscale eddies exert different influences on the particle size composition.
Although this study did not include direct analysis of phytoplankton community composition, previous studies
570 have shown that cyclonic eddies could promote the growth and proliferation of large-sized phytoplankton, such as
diatoms, allowing them to become dominant within the community (Shih et al., 2020; Chenillat et al., 2024). These
larger phytoplankton are more prone to form aggregates through intercellular coagulation (Panaïotis et al., 2024),
thereby contributing to the generation of larger particles. Moreover, they provide a favorable food source for large
zooplankton (Mangolte et al., 2022), which were indeed observed in greater abundance at stations S11 and S12 in
575 this study (Supplementary Fig. 2c). Together, these mechanisms likely contributed to the higher proportion of large
particles in the total PVC in the cyclonic eddy region at stations S11 and S12. In contrast, anticyclonic eddies,
characterized by nutrient depletion, tend to favor the proliferation of smaller phytoplankton groups, such as
picophytoplankton (Dai et al., 2020; Zhang et al., 2023). Compared to diatoms and other large phytoplankton
groups, picophytoplankton are less likely to form aggregates through cell coagulation (Guidi et al., 2009). Instead,
580 they are more readily consumed by small zooplankton such as ciliates, channeling biomass into the microbial loop
rather than into fast-sinking particles (Honjo et al., 2008). The abundance of large zooplankton at stations S4 and
S5 was also relatively low (Supplementary Fig. S2a, b). These conditions weaken the formation of large particles
here, thereby contributing to the increased proportion of small particles. Therefore, cyclonic and anticyclonic

eddies in the SCS exert different influences on particle concentration and size composition by altering nutrient availability and phytoplankton production processes. Cyclonic eddies tend to promote the formation of large particles, while anticyclonic eddies are associated with an increased proportion of small particles.

How do changes in particle concentration and size composition between cyclonic and anticyclonic eddy regions affect POC export flux? In this study, we applied the method proposed by Guidi et al. (2008a), which estimates POC flux from UVP-derived particle size spectra using an empirical relationship originally developed from a global sediment trap dataset. This method has since been widely applied across various oceanic regions for consistency and comparability (Ramondenc et al., 2016; Clements et al., 2023; Wang et al., 2004a). We acknowledge that regional differences may influence the absolute values of the estimated fluxes, the method remains robust for evaluating relative differences among stations within this study. In terms of carbon flux, the POC export at the cyclonic eddy influenced stations (S11 and S12) was significantly higher than that at the anticyclonic eddy influenced stations (S4 and S5) (Fig. 8a, *t*-test, $p < 0.01$). This difference was pronounced in the upper water column. For example, at 50 m depth, the POC flux at station S11 reached as high as $122 \text{ mg C m}^{-2} \text{ d}^{-1}$, while values at stations S4 and S5 were only 37 and $52 \text{ mg C m}^{-2} \text{ d}^{-1}$, respectively (Fig. 8a). A similar pattern was observed in the mesopelagic layer below 200 m, where fluxes at S11 and S12 remained markedly higher than those at S4 and S5. Quantitatively, the POC flux in the cyclonic eddy region was more than twice that in the anticyclonic eddy region. Cyclonic eddies can enhance POC export by stimulating primary productivity in the upper water column, whereas anticyclonic eddies tend to suppress it (Li et al., 2017; Zhang et al., 2020; Zhou et al., 2020). The significant correlation observed in this study between POC flux and Chl *a* (Fig. 9) further supports this relationship, indicating that increased phytoplankton biomass due to mesoscale processes is conducive to higher carbon export. An additional insight of this study is that the contribution of small particles to the POC flux was higher in the anticyclonic eddy influenced region compared to the cyclonic eddy influenced region, whereas the opposite pattern was observed for large particles (Fig. 8b, c). This pattern highlights the distinct export pathways associated with different eddy regimes. In anticyclonic eddies, although small particles still contribute less to the POC flux than large particles, their relative contribution is noticeably higher compared to that in cyclonic eddies. In contrast, cyclonic eddies enhance the formation of large, fast-sinking particles (Fig. 6), leading to a reduced proportional contribution of small particles to vertical carbon export. These findings emphasize the role of eddy polarity in shaping not only carbon flux magnitude, but also its particle size structure. These findings provide important implications for carbon export modeling. Most biogeochemical models assume a uniform particle sinking behavior or rely on bulk POC estimates, potentially underestimating the variability introduced by mesoscale physical processes (Bisson et al., 2018; Nowicki et al., 2022). Our findings emphasize the need for incorporating size-resolved particle fluxes and eddy-specific dynamics into carbon export models, particularly in regions where eddy activity is intense and persistent. Accounting for the contributions of particles with different size under varying eddy regimes will improve model accuracy in representing depth-dependent carbon attenuation and export efficiency.

5 Conclusion

This study represents one of the first efforts to apply high-resolution, size-resolved observations from the UVP5-HD to investigate depth-dependent particle distributions and carbon export dynamics along the continental slope of the SCS. Using high-resolution *in situ* observations from the UVP, this study provides a detailed characterization of particle distributions and particle-mediated carbon fluxes along the continental slope of the

625 SCS. The results ~~reveal~~demonstrate distinct spatial and vertical ~~heterogeneity~~patterns in particle distribution, ~~size~~structure, and POC flux, ~~strongly modulated by mesoscale eddy activity and size composition along the SCS slope,~~
630 ~~and elucidate the mechanisms by which mesoscale eddy processes influence particle characteristics and associated~~
~~carbon export fluxes.~~ Cyclonic eddies were associated with elevated particle concentrations, enhanced
contributions from large particles, and significantly higher POC fluxes throughout the upper and mesopelagic
layers. In contrast, anticyclonic eddies exhibited a higher proportion of small particles and reduced carbon export
efficiency.

Although small particles dominated numerically, large particles—due to their greater volume and faster
sinking velocities—contributed disproportionately to the total carbon flux. These findings demonstrate the
importance of resolving particle size composition when evaluating the biological carbon pump. By coupling UVP-
635 derived observations with eddy-resolved physical features, this study provides novel insights into the mechanisms
linking mesoscale processes to particle-mediated export, and enhances our understanding of carbon transport
dynamics in oligotrophic marginal seas like the SCS. Both particle abundance and volume concentration were
elevated at the inner slope stations and in the cyclonic eddy-influenced region, while lower values were observed
in other regions. In terms of size composition, small particles (ESD < 500 μm) overwhelmingly dominated in
640 numerical abundance throughout the water column, whereas large particles (ESD ≥ 500 μm) contributed
disproportionately to the particle volume concentration and POC flux. Although small particles numerically
dominate, their relatively lower volume and slower sinking rates limit their contribution to vertical POC export
compared to large particles. In terms of mesoscale eddy influence, our observations revealed pronounced
differences in particle characteristics and their associated carbon export between cyclonic and anticyclonic eddies.
645 Cyclonic eddies were associated with elevated particle concentrations, a reduced proportion of small particles, and
an increased contribution of large particles. In contrast, anticyclonic eddies showed a higher proportion of small
particles and a reduced share of large particles. These differences are primarily driven by eddy-induced changes
in upper-layer nutrient availability and phytoplankton production. Consequently, the POC flux in cyclonic eddy-
influenced regions was consistently higher than in anticyclonic regions throughout the water column.

650 This study represents one of the first efforts to apply size-resolved UVP observations to characterize depth-
dependent particle fluxes in the SCS. By resolving the relative roles of small and large particles and linking their
export patterns to mesoscale forcing, our results provide new insights into the size-selective processes governing
vertical carbon transport in marginal seas. These findings highlight the value of combining optical imaging tools
to constrain particle-mediated carbon export, which offers evidence that can inform the representation of size-
655 structured export fluxes in global biogeochemical models.

Data Availability Statement

Data available on request from the authors.

Author Contribution

660 SG: Conceptualization, Data curation, Formal analysis, Methodology, Software, Visualization, Writing-original
draft preparation. MZ: Data curation, Formal analysis, Investigation, Methodology, Validation. WX: Data curation,
Methodology. SZ: Investigation. SL: Data curation, Investigation. YW: Data curation, Investigation. JD: Data
curation. CZ: Visualization. XS: Conceptualization, Data curation, Funding acquisition, Project administration,

带格式的: 字体: Times New Roman

Supervision, Writing-review&editing.

Competing interests

665 The authors declare that they have no conflict of interest.

Disclaimer

Publisher's note: Copernicus Publications remains neutral with regard to jurisdictional claims made in the text, published maps, institutional affiliations, or any other geographical representation in this paper. While Copernicus Publications makes every effort to include appropriate place names, the final responsibility lies with
670 the authors.

Acknowledgements

We thank the crew and captain of the R/V *Nanfeng* for the logistic support during the cruise. [We thank Dr. Chuanjun Du for his assistance with data analysis.](#) This work was supported by the National Key Research and Development Program of China (No. 2024YFE0114300), the National Natural Science Foundation of China (No. 32371619,
675 U2006206), the National Basic Research Program of China (No. 2014CB441504), the International Partnership Program of Chinese Academy of Sciences (No. 133137KYSB20200002, 121311KYSB20190029).

Financial support

This research has been supported by the National Key Research and Development Program of China (No. 2024YFE0114300), the National Natural Science Foundation of China (No. 32371619, U2006206), the National
680 Basic Research Program of China (No. 2014CB441504), the International Partnership Program of Chinese Academy of Sciences (No. 133137KYSB20200002, 121311KYSB20190029).

References

- Accardo, A., Laxenaire, R., Baudena A., Speich, S., Kiko, R., Stemman, L.: Intense and localized export of selected marine snow types at eddy edges in the South Atlantic Ocean, *Biogeosciences*, 22, 1183–1201,
685 <https://doi.org/10.5194/bg-22-1183-2025>, 2025.
- Barlow, R., Lamont, T., Morris, T., Sessions, H., van den Berg, M.: Adaptation of phytoplankton communities to mesoscale eddies in the Mozambique Channel. *Deep-Sea Res. PT II*, 100, 106–118,
<https://doi.org/10.1016/j.dsr2.2013.10.020>, 2014.
- Barone, B., Church, M. J., Dugenne, M., Hawco, N. J., Jahn, O., White, A. E., John, S. G., Follows, M. J.,
690 DeLong, E. F., Karl, D. M.: Biogeochemical dynamics in adjacent mesoscale eddies of opposite polarity. *Global Biogeochem. Cy.*, 36(2), e2021GB007115, <https://doi.org/10.1029/2021GB007115>, 2022.
- ~~Bisson, K. M., Siegel, D. A., DeVries, T., Cael, B. B., Buesseler, K. O.: How data set characteristics influence ocean carbon export models. *Global Biogeochem. Cy.*, 32(9), 1312–1328,
<https://doi.org/10.1029/2018GB005934>, 2018.~~
- 695 Boss, E., Guidi, L., Richardson, M. J., Stemann, L., Gardner, W., Bishop, J. K., Anderson, R. F., Sherrell, R.

- M.: Optical techniques for remote and in-situ characterization of particles pertinent to GEOTRACES. *Prog. Oceanogr.*, 133, 43–54, <https://doi.org/10.1016/j.poccean.2014.09.007>, 2015.
- Boyd, P. W., Claustre, H., Levy, M., Siegel, D. A., Weber, T.: Multi-faceted particle pumps driven carbon sequestration in the ocean. *Nature*, 568(7752), 327–335, <https://doi.org/10.1038/s41586-019-1098-2>, 2019.
- 700 Buongiorno Nardelli, B., Droghei, R., Santoleri, R.: Multi-dimensional interpolation of SMOS sea surface salinity with surface temperature and in situ salinity data. *Remote Sens. Environ.*, 180, 392–402, <http://dx.doi.org/10.1016/j.rse.2015.12.052>, 2016.
- Chen, T., Liu, X. L., Bian, C. W., Zhang, S. T., Ji, C. S., Wu, Z. S., Jia, Y. G.: Nepheloid layer structure and variability along the highly energetic continental margin of the northern South China Sea. *J. Geophys. Res.*, 705 129(2), e2023JC020072, <https://doi.org/10.1029/2023JC020072>, 2024.
- Chenillat, F., Deshaies, E., Arens, A., Penven, P.: Role of mesoscale eddies in the biogeochemistry of the Mozambique Channel. *Front. Mar. Sci.*, 11, 1402776, doi: 10.3389/fmars.2024.1402776, 2024.
- Clements, D. J., Yang, S., Weber, T., McDonnell, A. M. P., Kiko, R., Stemmann, L., Bianchi, D.: New estimate of organic carbon export from optical measurements reveals the role of particle size distribution and export horizon. 710 *Global Biogeochem. Cy.*, 37, e2022GB007633, <https://doi.org/10.1029/2022GB007633>, 2023.
- Cram, J. A., Weber, T., Leung, S. W., McDonnell, A. M., Liang, J. H., Deutsch, C.: The role of particle size, ballast, temperature, and oxygen in the sinking flux to the deep sea. *Global Biogeochem. Cy.*, 32(5), 858–876, <https://doi.org/10.1029/2017GB005710>, 2018.
- Cram, J. A., Fuchsman, C. A., Duffy, M. E., Pretty, J. L., Lekanoff, R. M., Neibauer, J. A., Leung, S. W., 715 Huebert, K. B., Weber, T. S., Bianchi, D., Evans, N., Devol, A. H., Keil, R. G., McDonnell, A. M. P.: Slow particle remineralization, rather than suppressed disaggregation, drives efficient flux transfer through the eastern tropical North Pacific oxygen deficient zone. *Global Biogeochem. Cy.*, 36, e2021GB007080, <https://doi.org/10.1029/2021GB007080>, 2022.
- Dai, S., Zhao, Y. F., Liu, H. J., Hu, Z. Y., Zheng, S., Zhu, M. L., Guo, S. J., Sun, X. X.: The effects of a warm-core eddy on chlorophyll *a* distribution and phytoplankton community structure in the northern South China Sea in spring 2017. *J. Marine Syst.*, 210, 103396, <https://doi.org/10.1016/j.jmarsys.2020.103396>, 2020.
- Durkin, C. A., Estapa, M. L., Buesseler, K. O.: Observations of carbon export by small sinking particles in the upper mesopelagic. *Mar. Chem.*, 175, 72–81, <https://doi.org/10.1016/j.marchem.2015.02.011>, 2015.
- Fender, C. K., Kelly, T. B., Guidi, L., Ohman, M. D., Smith M, C., Stukel, M. R.: Investigating particle size-flux 725 relationships and the biological pump across a range of plankton ecosystem states from coastal to oligotrophic. *Front. Mar. Sci.*, 6, 603, <https://doi.org/10.3389/fmars.2019.00603>, 2019.
- Forest, A., Stemmann, L., Picheral, M., Burdorf, L., Robert, D., Fortier, L., Babin, M.: Size distribution of particles and zooplankton across the shelf-basin system in southeast Beaufort Sea: combined results from an Underwater Vision Profiler and vertical net tows. *Biogeosciences*, 9, 1301–1320, <https://doi.org/10.5194/bg-9-1301-2012>, 2012.
- 730 González-Estrada, E., Cosmes, W.: Shapiro–Wilk test for skew normal distributions based on data transformations. *J. Stat. Comput. Sim.*, 89, 3258–3272, <https://doi.org/10.1080/00949655.2019.1658763>, 2019.
- Gorsky, G., Picheral, M., Stemmann, L.: Use of the Underwater Video Profiler for the study of aggregate dynamics in the North Mediterranean. *Estuar. Coast. Shelf S.*, 50, 121–128, 735 <https://doi.org/10.1006/ecss.1999.0539>, 2000.
- Guidi, L., Stemmann, L., Legendre, L., Picheral, M., Prieur, L., Gorsky, G: Vertical distribution of aggregates

- (>100 μm) and mesoscale activity in the Northeastern Atlantic: effects on the deep vertical export of surface carbon. *Limnol. Oceanogr.*, 52, 7–18, <https://doi.org/10.4319/lo.2007.52.1.0007>, 2007.
- 740 Guidi, L., Jackson, G. A., Stemann, L., Miquel, J. C., Picheral, M., Gorsky, G.: Relationship between particle size distribution and flux in the mesopelagic zone. *Deep-Sea Res. PT I*, 55, 1364–1374, <https://doi.org/10.1016/j.dsr.2008.05.014>, 2008a.
- Guidi, L., Gorsky, G., Claustre, H., Miquel, J. C., Picheral, M., Stemann, L.: Distribution and fluxes of aggregates >100 μm in the upper kilometer of the South-Eastern Pacific. *Biogeosciences*, 5, 1361–1372, <https://doi.org/10.5194/bg-5-1361-2008>, 2008b.
- 745 Guidi, L., Stemann, L., Jackson, G. A., Ibanez, F., Claustre, H., Legendre, L., Picheral, M., Gorsky, G.: Effects of phytoplankton community on production, size, and export of large aggregates: a world-ocean analysis. *Limnol. Oceanogr.*, 54(6), 1951–1963, <https://doi.org/10.4319/lo.2009.54.6.1951>, 2009.
- Guidi, L., Calil, P. H. R., Duhamel, S., Björkman, K. M., Doney, S. C., Jackson, G. A., Li, B. L., Church, M. J., Tozzi, S., Kolber, Z. S., Richards, K. J., Fong, A. A., Letelier, R. M., Gorsky, G., Stemann, L., Karl, D. M.: Does eddy-eddy interaction control surface phytoplankton distribution and carbon export in the North Pacific Subtropical Gyre? *J. Geophys. Res.*, 117, G02024, <https://doi.org/10.1029/2012JG001984>, 2012.
- 750 Guidi, L., Legendre, L., Reygondeau, G., Uitz, J., Stemann, L., Henson, S. A.: A new look at ocean carbon remineralization for estimating deepwater sequestration. *Global Biogeochem. Cy.*, 29(7), 1044–1059, <https://doi.org/10.1002/2014GB005063>, 2015.
- 755 Guidi, L., Chaffron, S., Bittner, L., Eveillard, D., Larhlimi, A., Roux, S., Darzi, Y., Audic, S., Berline, L., Brum, J. R., Coelho, L. P., Espinoza, J. C. I., Malviya, S., Sunagawa, S., Dimier, C., Kandels-Lewis, S., Picheral, M., Poulain, J., Searson, S., Consortium Coordinators, T. O., Stemann, L., Not, F., Hingamp, P., Speich, S., Follows, M., Karp-Boss, L., Boss, E., Ogata, H., Pesant, S., Weissenbach, J., Wincker, P., Acinas, S. G., Bork, P., de Vargas, C., Iudicone, D., Sullivan, M. B., Raes, J., Karsenti, E., Bowler, C., Gorsky, G.: Plankton networks driving carbon export in the oligotrophic ocean. *Nature*, 532, 465–470, <https://doi.org/10.1038/nature16942>, 2016.
- Guo, M. X., Chai, F., Xiu, P., Li, S. Y., Rao, S.: Impacts of mesoscale eddies in the South China Sea on biogeochemical cycles. *Ocean Dynam.*, 65, 1335–1352, <https://doi.org/10.1007/s10236-015-0867-1>, 2015.
- 765 Honjo, S., Manganini, S. J., Krishfield, R. A., Francois, R.: Particulate organic carbon fluxes to the ocean interior and factors controlling the biological pump: A synthesis of global sediment trap programs since 1983. *Prog. Oceanogr.*, 76, 217–285, <https://doi.org/10.1016/j.pocan.2007.11.003>, 2008.
- Harms, N. C., Lahajnar, N., Gaye, B., Rixen, T., Schwarz-Schampera, U., Emeis, K.: Sediment trap-derived particulate matter fluxes in the oligotrophic subtropical gyre of the South Indian Ocean. *Deep-Sea Res. PT I*, 183, 104924, <https://doi.org/10.1016/j.dsr.2020.104924>, 2021.
- 770 Hays, G. C.: A review of the adaptive significance and ecosystem consequences of zooplankton diel vertical migrations. *Hydrobiologia*, 503, 163–170. <https://doi.org/10.1023/B:HYDR.0000008476.23617.b0>, 2003.
- Iversen, M. H., Nowald, N., Ploug, H., Jackson, G. A., Fischer, G.: High resolution profiles of vertical particulate organic matter export off Cape Blanc, Mauritania: degradation processes and ballasting effects. *Deep-Sea Res. PT I*, 57(6), 771–784, <https://doi.org/10.1016/j.dsr.2010.03.007>, 2010.
- 775 James, R.: Applications of the Underwater Vision Profiler for particle annotation in the oligotrophic North Pacific subtropical gyre, M.S. thesis, University of Hawai at Manoa, USA, 63 pp., 2024.

域代码已更改

带格式的: 超链接, 字体: (默认) Times New Roman, 10 磅, 字体颜色: 自动设置, 图案: 清除

- Jia, Y. G., Tian, Z. C., Shi, X. F., Liu, J. P., Chen, J. X., Liu, X. L., Ye, R. J., Ren, Z. Y., Tian, J. W.: Deep-sea sediment resuspension by internal solitary waves in the northern South China Sea. *Sci. Rep.*, 9, 12137, <https://doi.org/10.1038/s41598-019-47886-y>, 2019.
- 780 Jin, Y., Jin, M., Wang, D., Dong, C.: Statistical analysis of multi-year South China Sea eddies and exploration of eddy classification. *Remote Sens.*, 16, 1818, <https://doi.org/10.3390/rs16101818>, 2024.
- Jouandet, M. P., Trull, T. W., Guidi, L., Picheral, M., Ebersbach, F., Stemmann, L., Blain, S.: Optical imaging of mesopelagic particles indicates deep carbon flux beneath a natural iron-fertilized bloom in the Southern Ocean. *Limnol. Oceanogr.*, 56(3), 1130–1140, <https://doi.org/10.4319/lo.2011.56.3.1130>, 2011.
- 785 Jouandet, M. P., Jackson, G. A., Carlotti, F., Picheral, M., Stemmann, L., Blain, S.: Rapid formation of large aggregates during the spring bloom of Kerguelen Island: observations and model comparisons. *Biogeosciences*, 11, 4393–4406, <https://doi.org/10.5194/bg-11-4393-2014>, 2014, 2014.
- Kahru, M., Mitchell, B. G., Gille, S. T., Hewes, C. D., Holm-Hansen, O.: Eddies enhance biological production in the Weddell-Scotia Confluence of the Southern Ocean. *Geophys. Res. Lett.*, 34, L14603, <https://doi.org/10.1029/2007GL030430>, 2007.
- 790 Kiko, R., Biastoch, A., Brandt, P., Cravatte, S., Hauss, H., Hummels, R., Kriest, I., Marin, F., MaDonnell, A. M. P., Oschlies, A., Picheral, M., Schwarzkopf, F. U., Thurnherr, A. M., Stemmann, L.: Biological and physical influences on marine snowfall at the equator. *Nat. Geosci.*, 10(11), 852–858, <https://doi.org/10.1038/ngeo3042>, 2017.
- 795 Kiko, R., Picheral, M., Antoine, D., Babin, M., Berline, L., Biard, T., Boss, E., Brandt, P., Carlotti, F., Christiansen, S., Coppola, L., de la Cruz, L., Diamond-Riquier, E., de Madron, X. D., Elineau, A., Gorsky, G., Guidi, L., Hauss, H., Irisson, J. O., Karp-Boss, L., Karstensen, J., Kim, D., Lekanoff, R. M., Lombard, F., Lopes, R. M., Marec, C., McDonnell, A. M. P., Niemeyer, D., Noyon, M., O'Daly, S. H., Ohman, M. D., Pretty, J. L., Rogge, A., Searson, S., Shibata, M., Tanaka, Y., Tanhua, T., Taucher, J., Trudnowska, E., Turner, J. S., Waite, A., Stemmann, L.: A global marine particle size distribution dataset obtained with the Underwater Vision Profiler 5. *Earth Syst. Sci. Data*, 14, 4315–4337, <https://doi.org/10.5194/essd-14-4315-2022>, 2022.
- 800 Kriest, I.: Different parameterizations of marine snow in a 1D-model and their influence on representation of marine snow, nitrogen budget and sedimentation. *Deep-Sea Res. PT I*, 49(12), 2133–2162, [https://doi.org/10.1016/S0967-0637\(02\)00127-9](https://doi.org/10.1016/S0967-0637(02)00127-9), 2002.
- 805 Li, H. L., Wiesner, M. G., Chen, J. F., Ling, Z., Zhang, J. J., Ran, L. H.: Long-term variation of mesopelagic biogenic flux in the central South China Sea: Impact of monsoonal seasonality and mesoscale eddy. *Deep-Sea Res. PT I*, 126, 62–72, <https://doi.org/10.1016/j.dsr.2017.05.012>, 2017.
- Liu, H. J., Zhu, M. L., Guo, S. J., Zhao, X. H., Sun, X. X.: Effects of an anticyclonic eddy on the distribution and community structure of zooplankton in the South China Sea northern slope. *J. Marine Syst.*, 205, 103311, <https://doi.org/10.1016/j.jmarsys.2020.103311>, 2020.
- 810 Liu, J. A., Du, J. Z., Wu, Y., Liu, S. M.: Radium-derived water mixing and associated nutrient in the northern South China Sea. *Front. Mar. Sci.*, 9, 874547, <https://doi.org/10.3389/fmars.2022.874547>, 2022.
- Liu, Z. F., Zhao, Y. L., Colin, C., Statterger, K., Wiesner, M. G., Huh, C. A., Zhang, Y. W., Li, X. J., Sompongchaiyakul, P., You, C. F., Huang, C. Y., Liu, J. T., Siringan, F. P., Le, K. P., Sathiamurthy, E., Hantoro, W. S., Liu, J. G., Tuo, S. T., Zhao, S. H., Zhou, S. W., He, Z. D., Wang, Y. C., Bunsomboonsakul, S., Li, Y.: Source-to-sink transport processes of fluvial sediments in the South China Sea. *Earth-Sci. Rev.*, 153, 238–273, <https://doi.org/10.1016/j.earscirev.2015.08.005>, 2016.

Maiti, K., Benitez-Nelson, C. R., Rii, Y., Bidigare, R.: The influence of a mature cyclonic eddy on particle export in the lee of Hawaii. *Deep-Sea Res. PT II*, 55(10-13), 1445–1460, <https://doi.org/10.1016/j.dsr2.2008.02.008>, 2008.

820 Mangolte, I., Lévy, M., Dutkiewicz, S., Clayton, S. Jahn, O.: Plankton community response to fronts: winners and losers. *J. Plankton Res.*: 44(2), 241–258, <https://doi.org/10.1093/plankt/fbac010>, 2022.

McGillicuddy Jr., D. J.: Mechanisms of physical-biological-biogeochemical interaction at the oceanic mesoscale. *Annu. Rev. Mar. Sci.*, 8, 125–159, <https://doi.org/10.1146/annurev-marine-010814-015606>, 2016.

825 ~~Nowicki, M., DeVries, T., Siegel, D. A.: Quantifying the carbon export and sequestration pathways of the ocean's biological carbon pump. *Global Biogeochem. Cy.*, 36(3), e2021GB007083, <https://doi.org/10.1029/2021GB007083>, 2022.~~

Oliveira, A., Vitorino, J., Rodrigues, A., Jouanneau, J. M., Dias, J. A., Weber, O.: Nepheloid layer dynamics in the northern Portuguese shelf. *Prog. Oceanogr.*, 52(204), 195–213, [https://doi.org/10.1016/S0079-6611\(02\)00006-X](https://doi.org/10.1016/S0079-6611(02)00006-X), 2002.

830 Panaïotis, T., Poteau, A., Riquier, É. D., Catalano, C., Courchet, L., Motreuil, S., Coppola, L., Picheral, M., Irisson, J. O.: Temporal evolution of plankton and particles distribution across a mesoscale front during the spring bloom. *Limnol. Oceanogr.*, 9999, 1–15, <https://doi.org/10.1002/lno.12566>, 2024.

Peterson, T. D., Whitney, F. A., Harrison, P. J.: Macronutrient dynamics in an anticyclonic mesoscale eddy in the Gulf of Alaska. *Deep-Sea Res. PT II*, 52(7-8), 909–932, <https://doi.org/10.1016/j.dsr2.2005.02.004>, 2005.

835 Picheral, M., Guidi, L., Stemmann, L., Karl, D. M., Iddaoud, G., Gorsky, G.: The Underwater Vision Profiler 5: an advanced instrument for high spatial resolution studies of particle size spectra and zooplankton. *Limnol. Oceanogr-Meth.*, 8, 462–473, <https://doi.org/10.4319/lom.2010.8.462>, 2010.

Picheral, M., Colin, S., Irrison, J. O.: EcoTaxa, a tool for the taxonomic classification of images: available at: <http://ecotaxa.obs-vlfr.fr/http://ecopart.obs-vlfr.fr>, 2017.

840 Picheral, M., Catalano, C., Brousseau, D., Claustre, H., Coppola, L., Leymarie, E., Coindat, J., Dias, F., Fevre, S., Guidi, L., Irisson, J. O., Legendre, L., Lombard, F., Mortier, L., Penkerch, C., Rogge, A., Schmechtig, C., Thibault, S., Tixier, T., Waite, A., Stemmann, L.: The Underwater Vision Profiler 6: an imaging sensor of particle size spectra and plankton, for autonomous and cabled platforms. *Limnol. Oceanogr-Meth.*, 20(2), 115–129, <https://doi.org/10.1002/lom3.10475>, 2022.

845 Pretty, J. L.: Particles in the Pacific: how productivity and zooplankton relate to particles in the deep sea. M.S., thesis, University of Alaska Fairbanks, USA, 41 pp., 2019.

Ramondenc, S., Madeleine, G., Lombard, F., Santinelli, C., Stemmann, L., Gorsky, G., Guidi, L.: An initial carbon export assessment in the Mediterranean Sea based on drifting sediment traps and the underwater vision profiler data sets. *Deep-Sea Res. PT I*, 117, 107–119, <https://doi.org/10.1016/j.dsr.2016.08.015>, 2016.

850 Riley, J. S., Sanders, R., Marsay, C., Le Moigne, F. A. C., Achterberg, E. P., Poulton, A. J.: The relative contribution of fast and slow sinking particles to ocean carbon export. *Global Biogeochem. Cy.*, 26(1), <https://doi.org/10.1029/2011GB004085>, 2012.

Sammartino, M., Aronica, S., Santoleri, R., Nardelli, B. B.: Retrieving Mediterranean Sea surface salinity distribution and interannual trends from multi-sensor satellite and in situ data. *Remote Sens.*, 14, 2502, <https://doi.org/10.3390/rs14102502>, 2022.

855 Shih, Y. Y., Hung, C. C., Tuo, S. H., Shao, H. J., Chow, C. H., Muller, F. L. L., Cai, Y. H.: The impact of eddies on nutrient supply, diatom biomass and carbon export in the northern South China Sea. *Front. Earth Sc-Switz*, 8,

- 537332, <https://doi.org/10.3389/feart.2020.537332>, 2020.
- 860 Siegel, D. A., DeVries, T., Cetinić, I., Bisson, K. M.: Quantifying the ocean's biological pump and its carbon cycle impacts on global scales. *Annu. Rev. Mar. Sci.*, 15(1), 329–356, <https://doi.org/10.1146/annurev-marine-040722-115226>, 2022.
- Stamieszkin, K., Poulton, N. J., Pershing, A. J.: Zooplankton grazing and egestion shifts particle size distribution in natural communities. *Mar. Ecol. Prog. Ser.*, 575, 43–56, <https://doi.org/10.3354/meps12212>, 2017.
- 865 Stemmann, L., Eloire, D., Sciandra, A., Jackson, G. A., Guidi, L., Picheral, M., Gorsky, G.: Volume distribution for particles between 3.5 to 2000 μm in the upper 200 m region of the South Pacific Gyre. *Biogeosciences*, 5, 299–310, <https://doi.org/10.5194/bg-5-299-2008>, 2008.
- Stramma, L., Bange, H. W., Czeschel, R., Lorenzo, A., Frank, M.: On the role of mesoscale eddies for the biological productivity and biogeochemistry in the eastern tropical Pacific Ocean off Peru. *Biogeosciences*, 10, 7293–7306, <https://doi.org/10.5194/bg-10-7293-2013>, 2013.
- 870 Trudnowska, E., Lacour, L., Ardyna, M., Rogge, A., Irisson, J. O., Waite, A. M., Babin, M., Stemmann, L.: Marine snow morphology illuminates the evolution of phytoplankton blooms and determines their subsequent vertical export. *Nat. Commun.*, 12, 2816, <https://doi.org/10.1038/s41467-021-22994-4>, 2021.
- Trudnowska, E., Błachowiak-Samolyk, K., Stemmann, L.: Structures of coexisting marine snow and zooplankton in coastal waters of Svalbard (European Arctic). *Elem. Sci. Anth.*, 11(1), 00010, <https://doi.org/10.1525/elementa.2023.00010>, 2023.
- 875 Turner, J. T.: Zooplankton fecal pellets, marine snow, phytodetritus and the ocean's biological pump. *Prog. Oceanogr.*, 130, 205–248, <https://doi.org/10.1016/j.pocean.2014.08.005>, 2015.
- Turner, J. S., Pretty, J. L., McDonnell, A. M. P.: Marine particles in the Gulf of Alaska shelf system: Spatial patterns and size distributions from in situ optics. *Cont. Shelf Res.*, 145, 13–20, <https://doi.org/10.1016/j.csr.2017.07.002>, 2017.
- 880 Wang, L., Huang, B. Q., Chiang, K. P., Liu, X., Chen, B. Z., Xie, Y. Y., Xu, Y. P., Hu, J. Y., Dai, M. H.: Physical-biological coupling in the western South China Sea: the response of phytoplankton community to a mesoscale cyclonic eddy. *Plos One*, 11(4), e0153735, <https://doi.org/10.1371/journal.pone.0153735>, 2016.
- 885 Wang, X. Y., Li, H. L., Zhang, J. J., Chen, J. F., Xie, X. H., Xie, W., Yin, K. D., Zhang, D. S., Ruiz-Pino, D., Kao, S. J.: Seamounts generate efficient active transport loops to nourish the twilight ecosystem. *Sci. Adv.*, 10(26), eadk6833, [10.1126/sciadv.adk68](https://doi.org/10.1126/sciadv.adk68), 2024a.
- Wang, Z. Y., Fang, C., Yang, C. H., Zhang, G. Y., Sun, D.: Latitudinal gradient and influencing factors of deep-sea particle export along the Kyushu-Palau Ridge in the Philippine Sea. *Sci. Total Environ.*, 906, 167460, <https://doi.org/10.1016/j.scitotenv.2023.167460>, 2024b.
- 890 Welschmeyer, N. A.: Fluorometric analysis of chlorophyll a in the presence of chlorophyll b and pheopigments. *Limnol. Oceanogr.*, 39(8), 1985–1992, <https://doi.org/10.4319/lo.1994.39.8.1985>, 1994.
- Wu, C. R., Chiang, T. L.: Mesoscale eddies in the northern South China Sea. *Deep-Sea Res. PT II*, 54(14-14), 1575–1588, <https://doi.org/10.1016/j.dsr2.2007.05.008>, 2007.
- 895 Xu, W. L., Wang, G. F., Xing, X. G., Cornec, M., Hayward, A., Chen, B. Z., Chen, X. H.: Mesoscale eddies drive phytoplankton-mediated biogeochemistry in the South China Sea. *J. Geophys. Res.*, 130(6), e2024JG008664, <https://doi.org/10.1029/2024JG008664>, 2025.
- Xiu, P., Chai, F., Shi, L., Xue, H., Chao, Y.: A census of eddy activities in the South China Sea during 1993–

2007. *J. Geophys. Res.*, 115, C03012, <https://doi.org/10.1029/2009JC005657>, 2010.
- 900 Zhang, M., Wu, Y., Wang, F. Q., Xu, D. F., Liu, S. M., Zhou, M.: Hotspot of organic carbon export driven by mesoscale eddies in the slope region of the northern South China Sea. *Front. Mar. Sci.*, 7, 444, <https://doi.org/10.3389/fmars.2020.00444>, 2020.
- Zhang, W. J., Zhang, C., Zheng, S., Chen, Y. Y., Zhu, M. L., Sun, X. X.: Distribution of picophytoplankton in the northern slope of the South China Sea under environmental variation induced by a warm eddy. *Mar. Pollut. Bull.*, 905 194, 115429, <https://doi.org/10.1016/j.marpolbul.2023.115429>, 2023.
- Zhou, K. B., Dai, M. H., Maiti, K., Chen, W. F., Chen, J. H., Hong, Q. Q., Ma, Y. F., Xiu, P., Wang, L., Xie, Y. Y.: Impact of physical and biogeochemical forcing on particle export in the South China Sea. *Prog. Oceanogr.*, 187, 102403, <https://doi.org/10.1016/j.pocean.2020.102403>, 2020.
- Zhou, K. B., Benitez-Nelson, C. R., Huang, J., Xiu, P., Sun, Z. Y., Dai, M. H.: Cyclonic eddies modulate 910 temporal and spatial decoupling of particulate carbon, nitrogen, and biogenic silica export in the North Pacific Subtropical Gyre. *Limnol. Oceanogr.*, 66(9), 3508–3522, <https://doi.org/10.1002/lno.11895>, 2021.